Precambrian Research 354 (2021) 106047

Contents lists available at ScienceDirect

Precambrian Research

journal homepage: www.elsevier.com/locate/precamres

Petrogenetic source and tectonic evolution of the Neoproterozoic Nagar Parkar Igneous Complex granitoids: Evidence from zircon Hf isotope and trace element geochemistry

Hafiz Ur Rehman [a,*], Tahseenullah Khan [b], Hao-Yang Lee [c], Sun-Lin Chung [c,d], M. Qasim Jan [e], Tehseen Zafar [f], Mamoru Murata [g]

[a] Graduate School of Science and Engineering, Kagoshima University, Kagoshima, Japan
[b] Department of Earth and Environmental Sciences, Bahria University, Islamabad, Pakistan
[c] Institute of Earth Sciences, Academia Sinica, Taipei, Taiwan
[d] Department of Geosciences, National Taiwan University, Taipei, Taiwan
[e] National Centre of Excellence in Geology, University of Peshawar, Peshawar, Pakistan
[f] State Key Laboratory of Ore Deposit Geochemistry, Institute of Geochemistry, Chinese Academy of Sciences, Guiyang 550081, China
[g] Department of Geosciences, Naruto University of Education, Tokushima 772-8502, Japan

ARTICLE INFO

Keywords:
Neoproterozoic era
Nagar Parkar Igneous Complex
zircon Hf isotope
Trace element geochemistry
Juvenile crust

ABSTRACT

We investigated zircons from the Nagar Parkar Igneous Complex (NPIC) Gray and Pink granites for hafnium isotope and trace elements geochemistry to elucidate their petrogenetic source and tectonic setting. The studied zircons are characterized by oscillatory zoning, contain micro-inclusions of apatite, monazite, xenotime, and plagioclase. Rare-earth elements of the Neoproterozoic (ca. 750 Ma) zircons are characterized by a positive slope from La to Lu, exhibit distinct positive Ce- and negative Eu-anomalies that suggest their crystallization in magma that was fractionating plagioclase. The relatively smaller but variable Ce/Ce^*_N ratios (2–62), smaller Eu/Eu^*_N (0.01 to 0.45), and comparatively higher Th/U ratios (>0.30, reaching up to 3.20) affirm their derivation mainly from the continental crustal type magmas. The εHf(t) values of zircons in Gray and Pink granites range from +5.7 to +14.4 and +1.9 to +10.7, respectively, indicate their derivation from a juvenile crust and the absence of negative εHf(t) values point towards non-involvement of the older or reworked material during the crustal growth. The T_{DM} model ages, calculated from the Hf isotope values of zircons, spread between 1119 and 736 Ma for Gray and 1013 and 900 Ma in Pink granites, further opine their derivation from a comparatively young and juvenile crust. Crystallization temperatures, estimated from the titanium content in zircon and zircon-saturation in whole-rock, range from 631 to 905 °C and 784 to 918 °C, respectively, show consistent results for the crystallization conditions of most granitic melts. Whole-rock major and trace element data, combined with zircon Hf isotope and trace elements geochemistry suggest within-plate A-type granitic magma that likely generated in a rift-related tectonic setting that persisted along the western margin of Rodinia during the Neoproterozoic era.

1. Introduction

A number of outcrops of the two types of granites, commonly referred to as Gray and Pink granites, are exposed in the Thar Desert, east of Karachi, Pakistan (Fig. 1a), that are collectively called as the Nagar Parkar Igneous Complex (NPIC). Gray granites are the dominant type whereas Pink granites occur locally in the surroundings of the former type. These igneous bodies are situated in the southwest of the Malani Igneous Suite (MIS) of Rajasthan in India (Fig. 1b) hence are correlative. Based on whole-rock major and trace elements geochemistry, the NPIC granitoids were thought to have resulted from the fractional crystallization of magma, partial melting of the continental crust during rifting or in an Andean-type tectonic setting (e.g. Jan et al., 2018; Khan et al., 2017 and references therein). Geochemical features and same ages of emplacement mark the NPIC granites to a large-scale magmatic province that produced the granitoids of MIS, Madagascar, Seychelles, and those exposed in the South China Block (Ashwal et al., 2002, 2013; Kochhar, 2004; Sharma, 2005; de Wall et al., 2018; Wang

* Corresponding author.
E-mail address: hafiz@sci.kagoshima-u.ac.jp (H.U. Rehman).

https://doi.org/10.1016/j.precamres.2020.106047
Received 1 September 2020; Received in revised form 20 November 2020; Accepted 2 December 2020
Available online 24 December 2020

et al., 2017; Shellnutt et al., 2020). Interpretations regarding the origin and tectonic settings of NPIC granites were based mainly on their regional correlation with the MIS, however, little is known regarding the petrogenetic source and magma genesis. In this study, we analyzed multiple zircon grains from both the Gray and Pink granites for trace element compositions combined with in-situ Hf isotope ratios, and present whole-rock major and trace element contents from several representative samples. As zircon is highly resistant to secondary processes (e.g. Hoskin and Ireland, 2000; Corfu et al., 2003; Hoskin, 2005; Belousova et al., 2002, 2006; Grimes et al., 2015), the pristine information it preserves provide insightful knowledge regarding the timing of magmatic crystallization and petrogenetic source. Moreover, Hf isotope data of zircon help further in elucidating the evolutionary processes of magma from which the granites are generated. Therefore, combining the textural features with geochemical compositions and age-data help in assigning the petrogenetic source and spatial evolution. As mentioned above, zircon is faithful recorder of its precursor tectono-thermal events, we investigated it with the aims (1) to identify the petrogenetic source and tectonic settings in which the NPIC granites formed, (2) the temperatures of crystallization, and (3) to elucidate magma evolution through space and time. Our data provide sufficient evidence for the petrogenetic source and tectonic evolution of the NPIC granitoids.

2. Geology

A number of Neoproterozoic (~750 Ma) granitic plutons are exposed some 200 km east of Karachi, Pakistan (Fig. 1a) that are collectively called as the Nagar Parkar Igneous Complex. These granites are generally situated to the west of the Malani Igneous Suite and both the above-mentioned areas share petrological and geochemical features (Fig. 1b). In the NPIC, riebeckite-aegirine Gray granites are the dominant type which are neighbored by biotite-hornblende Pink granites. The two granite varieties are emplaced within the metamorphic basement (mafic, tonalitic and rhyolitic rocks) that have experienced epidote–amphibolite- and greenschist-facies metamorphism. The granites and basement rocks are intruded by numerous felsic and mafic dykes. Gray granites are typified by plagioclase, quartz, riebeckite, aegirine, perthitic feldspar, and biotite with accessory apatite, monazite, and zircon. Pink granites are characterized by phenocrystic orthoclase embedded in plagioclase displaying the rapakivi texture. Other phases include biotite, hornblende, perthite, and quartz along with minor ilmenite, titanite, and magnetite. Accessory phases are comprised of apatite, monazite, and zircon. Detailed petrological, mineralogical, and field features have been reported in past publications (Jan et al., 1997, 2014; Khan et al., 2012, 2017; Rehman et al., 2018, and references therein).

3. Methods and results

3.1. Whole-rock major and trace element geochemistry

Major oxides (wt%) and trace element (ppm) contents (analyzed by XRF on fused glass beads and pressed-pellets) from representative samples of Gray and Pink granites are given in Table 1. The data from both granites plot indistinguishably within the fields of high-K calc-alkaline series (Fig. 2a) in bivariate plot of SiO_2 vs. K_2O (Peccerillo and Taylor, 1976). For comparison, whole-rock data of granites of the MIS (Eby and Kochhar, 1990; de Wall et al., 2018), Seychelles (Shellnutt et al., 2020), and Madagascar (Thomas et al., 2009) are also shown that plot in the same fields, suggesting their geochemical similarity. Other major and trace element discrimination diagrams distinguish these granites as A-type granitoids mainly ferroan (Fig. 2b: SiO_2 vs. FeO/FeO + MgO diagram of Frost et al., 2001). In the Al saturation index (A/CNK) diagram of Shand (1943), the granites plot in the peraluminous field, but with some transition towards the peralkaline field, defining a linear trend (Fig. 2c). Trace element discrimination diagrams (Rb vs. Y + Nb proposed by Pearce et al., 1984) depict within-plate and syn-collisional granitoids (Fig. 2d). Indeed, whole-rock major and trace element data

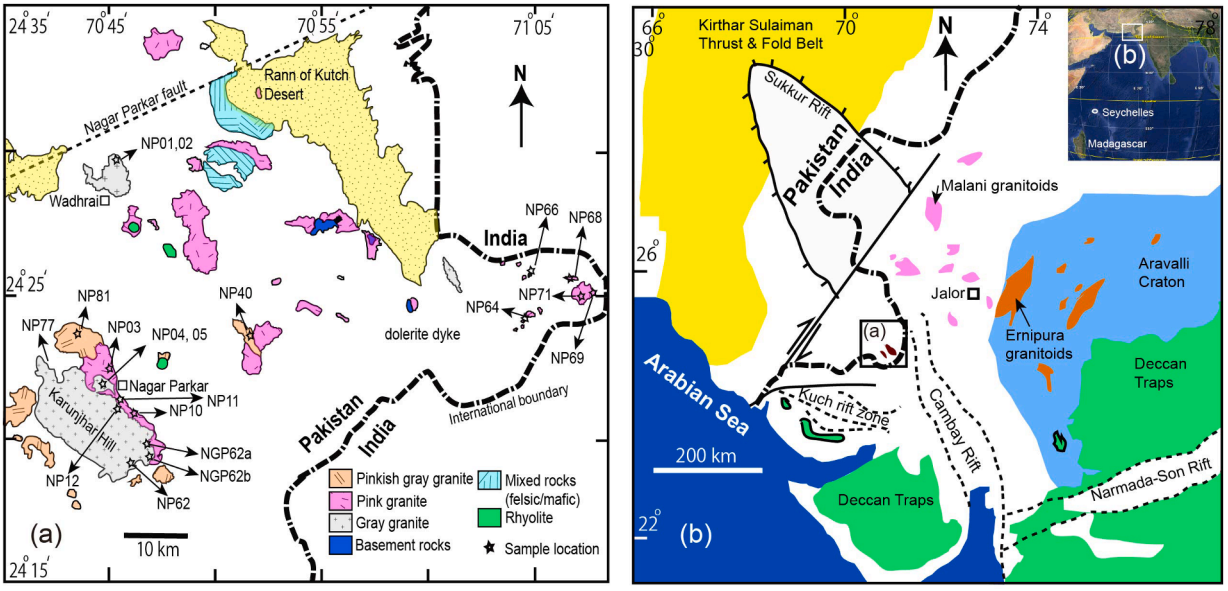

Fig. 1. (a) Simplified geological map of the Nagar Parkar Igneous Complex, showing the occurrence of Gray and Pink granites and other lithologies (map modified after Khan et al., 2012 and references therein). Stars indicate sample locations. (b) Geological sketch map of the NPIC and surrounding areas including that of the MIS of India (map modified after Khan et al., 2012 and references therein). Inset at the top is a Google Earth image showing the location of NPIC, MIS, Madagascar, and Seychelles. (For interpretation of the references to colour in this figure legend, the reader is referred to the web version of this article.)

Table 1
Major oxides (wt%) and trace elements (ppm) of the selected granites and felsic dykes of the Nagar Parkar Igneous Complex.

Rock	Gray granites								Pink granites								Porphyritic felsic dykes (Khan et al. 2017)				
Sample	NP40	NP81	NP4	NP5	NP12	NP77	NP1	NP2	NP64	NP66	NP68	NP69	NP71	NP3	NP10	NP11	PA2	VW100	NP15	NP61	NP78
SiO_2	77.22	77.20	77.02	77.36	76.90	77.34	73.86	73.55	76.19	75.05	76.52	75.95	76.36	78.34	77.65	77.59	78.03	76.64	78.47	74.27	71.64
TiO_2	0.17	0.17	0.20	0.20	0.18	0.16	0.33	0.33	0.23	0.33	0.24	0.29	0.26	0.10	0.09	0.09	0.15	0.18	0.2	0.35	0.44
Al_2O_3	12.26	12.33	11.51	11.42	11.71	11.59	13.86	14.12	12.11	12.47	12.28	12.02	12.25	11.87	12.24	12.06	12.32	12.6	11.91	12.89	12.89
FeO (t)	1.35	1.39	2.26	2.25	2.17	2.02	2.09	2.09	2.11	2.41	1.83	2.23	1.99	0.90	1.00	1.25	0.83	1.4	1.04	2.61	3.42
MnO	0.02	0.03	0.04	0.04	0.05	0.04	0.07	0.08	0.05	0.05	0.04	0.05	0.04	0.01	0.02	0.02	0.02	0.03	0.02	0.05	0.06
MgO	0.18	0.16	0.16	0.17	0.14	0.14	0.35	0.38	0.17	0.36	0.21	0.30	0.26	0.11	0.10	0.08	0.14	0.15	0.3	0.35	0.91
CaO	0.33	0.48	0.39	0.30	0.28	0.37	1.00	1.09	0.55	0.85	0.53	0.76	0.71	0.41	0.32	0.37	0.43	0.54	1.15	0.91	1.9
Na_2O	3.06	3.02	3.58	3.33	3.61	3.51	4.23	4.41	3.15	2.86	2.99	3.01	2.96	3.02	3.66	3.36	3.4	3.47	5.96	3.5	4.13
K_2O	4.98	4.94	4.66	4.67	4.74	4.62	3.83	3.60	5.21	5.26	5.17	5.04	5.02	4.82	4.41	4.72	4.65	4.98	0.06	4.69	3.9
P_2O_5							0.04	0.04	0.01	0.03	0.03	0.04	0.02				0.04	0.02	0.01	0.04	0.05
LOI	0.38	0.29	0.23	0.17	0.22	0.21	0.33	0.39	0.23	0.33	0.17	0.22	0.14	0.41	0.51	0.45			0.88	0.34	0.66
Total	99.95	100.01	100.05	99.91	100	100	99.99	100.08	100.01	100	100.01	99.91	100.01	99.99	100	99.99	100.01	100.01	100	100	100
Zr (ppm)	231.92	186.47	573.91	583.79	532.71	496.00	344.20	294.05	359.13	300.18	194.22	346.40	286.05	138.87	139.75	358.01	139.60	197.86	221.04	465.22	524.13
Nb	24.24	19.94	27.36	29.86	27.21	26.00	14.46	10.51	23.66	22.48	17.71	25.27	21.79	27.06	31.22	62.76	9.60	21.12	20.02	19.04	20.95
Y	61.60	57.44	70.42	70.72	74.49	75.00	49.65	42.30	64.73	58.19	48.59	59.34	54.80	69.54	75.05	91.10	30.03	46.87	39.03	57.13	56.98
Sr	41.30	33.66	13.79	18.03	17.15	13.00	99.40	118.91	30.24	59.95	50.10	48.70	55.42	13.82	14.64	12.55	32.60		85.75	54.86	59.02
Rb	126.12	120.91	104.60	102.79	108.41	107.00	87.90	81.31	109.34	116.28	121.98	109.23	115.45	147.71	137.62	157.56	110.90	151.01	BDL	85.04	70.20
Zn	48.29	41.47	119.62	121.14	130.46	110.00	87.22	55.05	89.45	76.60	63.30	74.46	64.66	33.91	40.88	49.46			42.79	84.04	111.01
Ba	232.22	238.73	156.58	142.55	166.24	176.00	726.29	797.19	112.85	177.40	204.78	189.18	186.94	49.55	42.70	46.68	233.50	117.01	BDL	346.05	450.03
Ce	100.03	113.98	154.16	137.38	102.00	152.00	110.43	99.61	164.55	118.71	154.21	141.67	149.62	128.88	70.69	68.44	77.80	110.01	113.97	177.01	157.12
Th	15.82	12.15	10.28	11.46	BDL	10.00	8.28	7.69	11.57	9.98	10.71	11.08	9.31	13.52	15.52	24.46	9.50	22.09	12.90	10.04	BDL
U																	4.02	4.02	5.03	3.01	4.02
Nd	43.54	59.07	70.24	60.61	45.00	15.00	52.12	41.24	68.57	68.94	50.68	51.37	49.11	44.39	37.31	44.35			41.02	55.06	60.09
Ga	24.85	23.29	27.65	27.60	28.45	29.00	22.17	20.61	25.28	24.75	24.01	24.34	24.13	25.48	29.46	27.76			20.96	26.05	26.01
Oxide wt%/Eq wt																					
Si O	1.286	1.285	1.282	1.288	1.280	1.288	1.230	1.225	1.269	1.250	1.274	1.265	1.271	1.304	1.293	1.292	1.299	1.276	1.307	1.237	1.193
Ti O	0.002	0.002	0.003	0.003	0.002	0.002	0.004	0.004	0.003	0.004	0.003	0.004	0.003	0.001	0.001	0.001	0.002	0.002	0.003	0.004	0.006
Al O	0.240	0.242	0.226	0.224	0.230	0.227	0.272	0.277	0.238	0.245	0.241	0.236	0.240	0.233	0.240	0.237	0.242	0.247	0.234	0.253	0.253
Fe O (t)	0.019	0.019	0.031	0.031	0.030	0.028	0.029	0.029	0.029	0.034	0.025	0.031	0.028	0.013	0.014	0.017	0.012	0.019	0.014	0.036	0.048
Mn O	0.000	0.000	0.001	0.001	0.001	0.001	0.001	0.001	0.001	0.001	0.001	0.001	0.001	0.000	0.000	0.000	0.000	0.000	0.000	0.001	0.001
Mg O	0.004	0.004	0.004	0.004	0.003	0.003	0.009	0.009	0.004	0.009	0.005	0.007	0.006	0.003	0.002	0.002	0.003	0.004	0.007	0.009	0.023
Ca O	0.006	0.009	0.007	0.005	0.005	0.007	0.018	0.019	0.010	0.015	0.009	0.014	0.013	0.007	0.006	0.007	0.008	0.010	0.021	0.016	0.034
Na O	0.099	0.097	0.116	0.107	0.116	0.113	0.136	0.142	0.102	0.092	0.096	0.097	0.095	0.097	0.118	0.108	0.110	0.112	0.192	0.113	0.133
K O	0.106	0.105	0.099	0.099	0.101	0.098	0.081	0.076	0.111	0.112	0.110	0.107	0.107	0.102	0.094	0.100	0.099	0.106	0.001	0.100	0.083
P O	0.000	0.000	0.000	0.000	0.000	0.000	0.001	0.001	0.000	0.000	0.000	0.001	0.000	0.000	0.000	0.000	0.001	0.000	0.000	0.001	0.001
Total	1.762	1.764	1.768	1.763	1.769	1.767	1.781	1.784	1.765	1.761	1.765	1.761	1.765	1.761	1.768	1.764	1.775	1.777	1.779	1.769	1.773
Cation fraction																					
Si	0.730	0.729	0.725	0.731	0.724	0.729	0.691	0.686	0.719	0.710	0.722	0.718	0.720	0.741	0.731	0.732	0.732	0.718	0.734	0.699	0.673
Ti	0.001	0.001	0.001	0.001	0.001	0.001	0.002	0.002	0.002	0.002	0.002	0.002	0.002	0.001	0.001	0.001	0.001	0.001	0.001	0.002	0.003
Al_2	0.136	0.137	0.128	0.127	0.130	0.129	0.153	0.155	0.135	0.139	0.136	0.134	0.136	0.132	0.136	0.134	0.136	0.139	0.131	0.143	0.143
Fe	0.011	0.011	0.018	0.018	0.017	0.016	0.016	0.016	0.017	0.019	0.014	0.018	0.016	0.007	0.008	0.010	0.007	0.011	0.008	0.021	0.027
Mn	0.000	0.000	0.000	0.000	0.000	0.000	0.001	0.001	0.000	0.000	0.000	0.000	0.000	0.000	0.000	0.000	0.000	0.000	0.000	0.000	0.000
Mg	0.003	0.002	0.002	0.002	0.002	0.002	0.005	0.005	0.002	0.005	0.003	0.004	0.004	0.002	0.001	0.001	0.002	0.002	0.004	0.005	0.013
Ca	0.003	0.005	0.004	0.003	0.003	0.004	0.010	0.011	0.006	0.009	0.005	0.008	0.007	0.004	0.003	0.004	0.004	0.005	0.012	0.009	0.019
Na_2	0.056	0.055	0.065	0.061	0.066	0.064	0.077	0.080	0.058	0.052	0.055	0.055	0.054	0.055	0.067	0.061	0.062	0.063	0.108	0.064	0.075
K_2	0.060	0.059	0.056	0.056	0.057	0.056	0.046	0.043	0.063	0.063	0.062	0.061	0.060	0.058	0.053	0.057	0.056	0.060	0.001	0.056	0.047
P_2	0.000	0.000	0.000	0.000	0.000	0.000	0.000	0.000	0.000	0.000	0.000	0.000	0.000	0.000	0.000	0.000	0.000	0.000	0.000	0.000	0.000
M	1.23	1.25	1.39	1.33	1.37	1.36	1.35	1.35	1.36	1.35	1.30	1.37	1.31	1.24	1.27	1.28	1.26	1.33	1.37	1.39	1.67
$D_{Zr}^{zircon/melt}$	2146	2669	867	852	934	1003	1446	1692	1386	1658	2562	1437	1740	3584	3561	1390	3565	2515	2251	1070	949

(*continued on next page*)

Table 1 (*continued*)

Rock	Gray granites								Pink granites							Porphyritic felsic dykes (Khan et al. 2017)				
Sample	NP40	NP81	NP4	NP5	NP12	NP77	NP1	NP2	NP64	NP66	NP68	NP69	NP71	NP3	NP10	NP11	PA2	VW100	NP15	NP61	NP78
T_{Zr_Sat}	***832***	***811***	***910***	***918***	***905***	***898***	***861***	***845***	***865***	***848***	***811***	***860***	***846***	***785***	***784***	***871***	***784***	***810***	***817***	***889***	***876***
	Gray granites								Pink Granites								Porphyritic dykes				
Average $T_{Zr\text{-}Sat}$	873								828								835				
Min	811								784								784				
Max	918								865								889				
Median	880								846								817				

Foot note to Table 1: Zr-saturation temperature values and related calculations are done based on the methods and calibrations of Watson and Harrison (1983) as [T = 12900/(LN($D_{Zr}^{zircon/melt}$) + 3.8 + 0.85*(M − 1))-273.15] where M is calculated as the cation fraction [$X_{Na} + X_K + 2X_{Ca}/X_{Si}*X_{Al}$] and D_{Zr} as 497647/Zr ppm.

give ample information for petrogenesis, however, secondary processes or local geochemical variations within a single pluton may affect the results and hence interpretations. Compared to whole-rock major and trace element geochemistry, zircon, a strong and resistant mineral to alteration, is a faithful recorder to preserve the primary information acquired from the parent magma during its crystallization. To better understand the petrogenetic source and evolution of the Neoproterozoic NPIC granitoids, we investigated zircons from five samples of Gray granite and one sample of Pink granite for trace elements (including REE) concentrations and in-situ Hf isotope ratios (see Fig. 1a for sample location). Those grains were earlier analyzed for U–Pb isotope ratios and both granites showed almost similar magmatic peak at ca. 750 Ma (Rehman et al., 2018). The age data are consistent with the previously conveyed results for the NPIC granitoids (Khan et al., 2012; Markhand et al., 2017; Mastoi et al., 2019), and comparable to the ages found from zircon or whole-rocks of granites from MIS (Crawford and Compston, 1969; Dhar et al., 1996; Meert et al., 2013; Chaudhuri et al., 2020), Seychelles (Shellnutt et al., 2020), and Madagascar (Eby and Kochhar, 1990; Torsvik et al., 2001a, 2001b; Ashwal et al., 2002, 2013).

Most of the studied zircon grains (Fig. 3) contained numerous inclusions of apatite, ilmenite, monazite, xenotime, and plagioclase, identified via the EDX-detector attached to the scanning electron microscope (SEM). Crystal morphology and internal structures were studied first using the optical microscope, followed by backscattered electron (BSE) and cathodoluminescence (CL) imaging obtained using the SEM.

Trace element analysis on zircons was conducted simultaneously with the U–Pb age dating, using the laser ablation inductively coupled plasma mass spectrometry (LA-ICP-MS) Agilent 7500s quadruple ICP-MS, with a Photon Machines Analyte G2 193 nm excimer laser ablation system, at National Taiwan University's Department of Geosciences. Analytical conditions and parameters of the LA-ICP-MS were adopted from those reported in past publications (Chiu et al., 2009; Rehman et al., 2016) and specifically those reported in Rehman et al. (2018). In each run(s) of U–Pb and trace element analysis, eight to ten measurements of unknown samples (zircons in this study) were performed, bracketed by the NIST 612 glass and several zircon reference materials (GJ-1 as the primary standard for mass discrimination and age correction, and 91,500 and Plešovice/PLS as the secondary standards for data quality control). Elemental concentrations were acquired from each analysis using the GLITTER software v. 4.4 (http://www.glitter-gemoc.com) installed on the LA-ICP-MS PC. Representative zircons with analyzed spots are shown in Fig. 4, and trace element concentrations are shown in Table 2 from selected grains in one Gray granite sample (NGP62a) whereas a complete set of analytical results (including the standards with detection limits and errors) are provided in supplementary Table S1 (available on-line). Entire lot of the analyzed zircons are provided in supplementary Fig. S2 (available on-line).

After the U–Pb and trace element simultaneous analysis, the same zircon grains were laser bombarded for Hf isotope ratios, using the Nu Plasma high resolution (HR) multi-collector (MC-) ICP-MS situated at the Institute of Earth Sciences, Academia Sinica, Taiwan. Laser ablation system was Photon Machines Analyte G2 193 nm excimer. Each analysis was performed using 120 s (first 30 s for the background noise elimination followed by ~ 85 s of the sample intensity) with a 50 μm beam diameter, 5–8 Hz repetition pulse rate, and ~8–9 J/cm^2 of laser energy. All the analyses were performed above the earlier ablated spots of the U–Pb and trace element analysis. For instrumental quality control, Mud Tank (MT) zircon was used as the primary external reference material that yielded an average $^{176}Hf/^{177}Hf$ value of 0.282498 ± 0.000030 (2σ, n = 22) during the analytical session whereas the long-term value was 0.282495 ± 0.000029 (2σ, n = 636). Secondary external reference materials used were Plešovice, 91,500 and TEMORA zircons which yielded long-term average $^{176}Hf/^{177}Hf$ values of 0.282483 ± 21 (2σ, n = 84), 0.282314 ± 23 (2σ, n = 40), and 0.282689 ± 30 (2σ, n = 42), respectively. The results are summarized in Table 3 and some of the

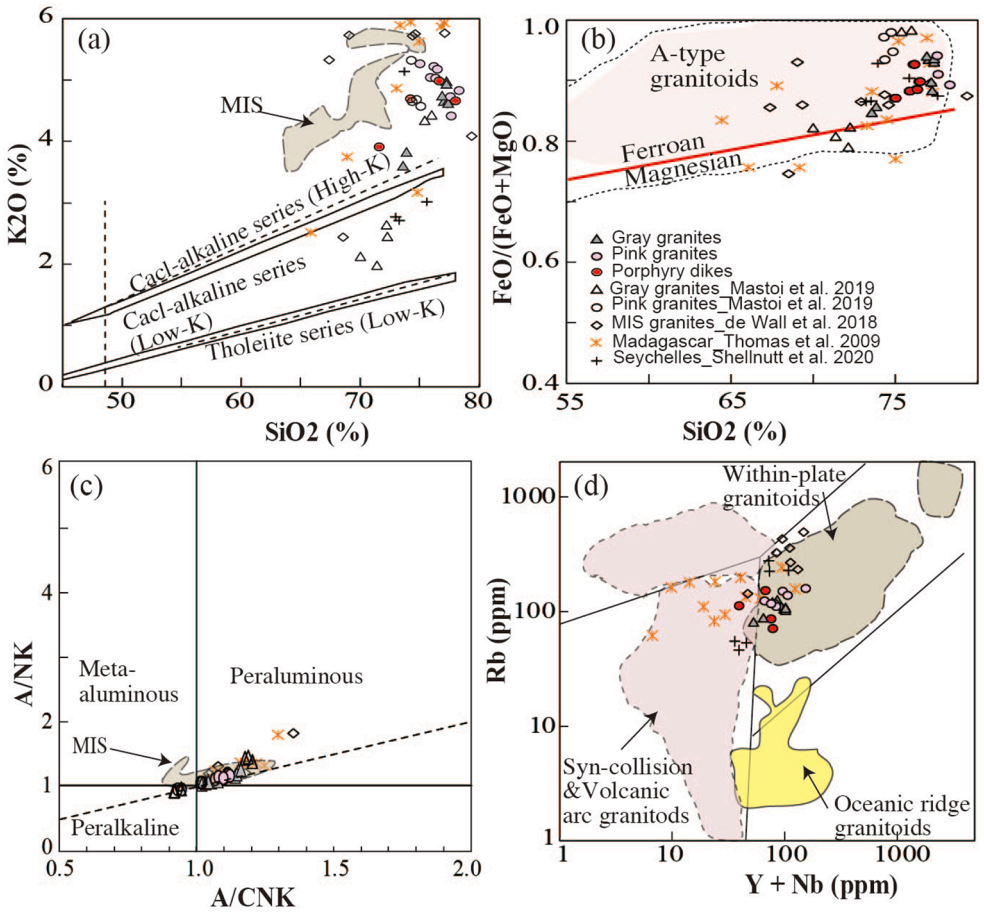

Fig. 2. Binary plots constructed from major and trace element contents or ratios of the whole-rock analyses from the NPIC, MIS, Madagascar and Seychelles. Data from different areas show significant geochemical similarity, indicating the~~ir~~ same magma source-region. (a) SiO_2 vs. K_2O plot after Peccerillo and Taylor, 1976. Data shown on the plots for the NPIC are from Khan et al. (2012) and Mastoi et al. (2019), for MIS from de Wall et al. (2018), for Madagascar from Thomas et al. (2009), and for Seychelles from Shellnutt et al. (2020). Gray field marked with MIS is data from Eby and Kochhar (1990), de Wall et al. (2012) and de Wall et al. (2014), (b) SiO_2 vs. FeO/(FeO/MgO) plot showing the NPIC and associated granitoids. Field encircled by the dotted line represent A-type granitoids from the well-known localities around the globe and the shaded area represents 95% analysis for the A-type granites, (c) A/CNK vs. A/NK plot after Shand (1943), and (d) Rb (ppm) vs. Y + Nb (ppm) plot, with fields for the syn-collision granites, volcanic arc granites, within-plate granites, and ocean ridge granites adopted from Pearce et al. (1984). Data from both Gray and Pink granites from the NPIC, and granites from the MIS, Madagascar, and Seychelles predominantly plot in the field of within-plate granitoids with a few samples from the Madagascar (Thomas et al., 2009) and Seychelles (Shellnutt et al., 2020) show some transition towards syn-collision granitoids. There are several other studies on the NPIC, MIS, Madagascar, and Seychelles (not shown on the plot) and chemical compositions from the granitoid samples are more or less similar. (For interpretation of the references to colour in this figure legend, the reader is referred to the web version of this article.)

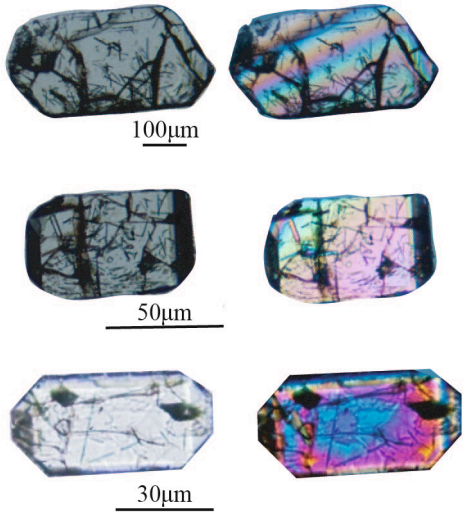

Fig. 3. Representative photomicrographs of euhedral and prismatic zircons separated from the NPIC granites.

representative spots are shown in Fig. 4. Detailed results and zircon images are given in supplementary Fig. S2 (available on-line).

3.2. *Trace element geochemistry of zircons*

In Gray granites, 30 spots were analyzed on zircons for trace elements in sample NGP62a (Table 2 and Fig. 4), 36 spots on zircons in sample NGP62b, 41 spots on zircons in sample NP62, 36 spots on zircons in Sample NP12, and 30 spots in zircons in sample NP01 (supplementary Table S1 & Fig. S2, available on-line). Similarly, 15 spots were analyzed on zircons in one Pink granite sample NP10.

Chondrite-normalized REE and trace-element data (McDonough and Sun, 1995) for the six samples are plotted in Fig. 5. The zircon REE data from both granites demonstrate identical pattern, with a positive slope from La to Lu, a prominent positive Ce-anomaly and distinct negative Eu-anomaly, a common feature of the magmatic zircons (Hoskin and Ireland, 2000; Corfu et al., 2003; Hoskin, 2005; Grimes et al., 2007). Several grains or domains within the zircons (sample NP12, NP01, and NP10) show relatively higher or elevated LREE compared with other grains within the same samples (Fig. 5). Those features may indicate the presence of LREE enriched inclusions (e.g. apatite, xenotime, and monazite) that were almost impossible to avoid during the laser ablation. The Ce/Ce* ratios (calculated as $CeN/\sqrt{LaN*PrN}$) vary between 2

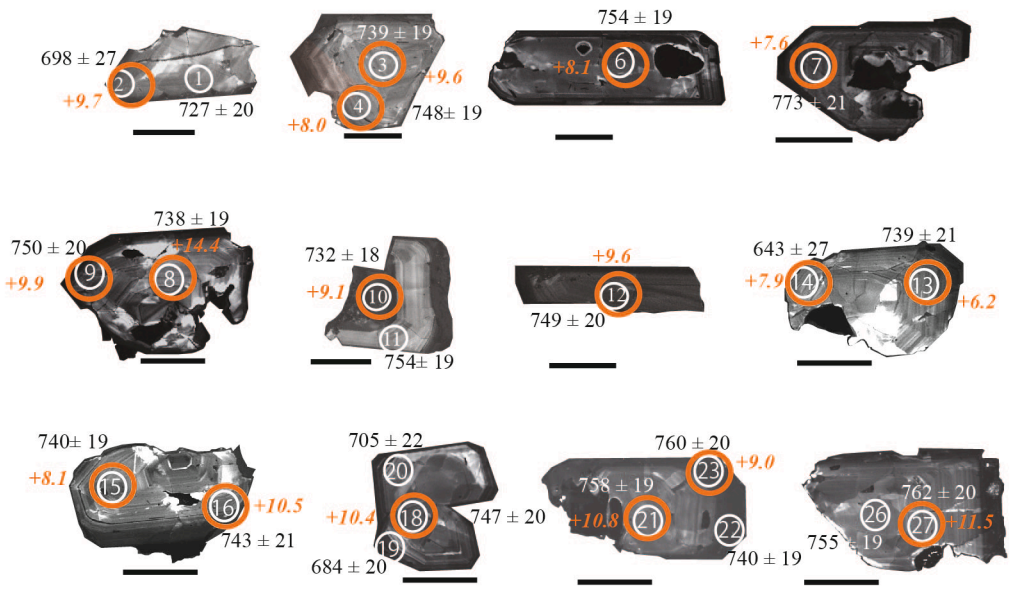

Fig. 4. Cathodoluminescence (CL) images of representative zircon grains from the NPIC Gray granite (Sample NGP62a). White circles with numbers represent the LA-ICP-MS U–Pb/trace element analyzed spots. Age data, reproduced from Rehman et al. (2018), with 1σ errors shown. Large circles above the trace element analysis spot represent Hf isotope analyses and the digits show the calculated εHf (t) values. For detailed results and analytical methods, see the text and Tables 2 and 3.

and 62 (average: 10). The Eu/Eu* ratios (calculated as $EuN/\sqrt{SmN + GdN}$) range from 0.01 to 0.45 (average: 0.16), while the Th/U ratios are relatively higher (>0.3, reaching up to 3.2). The REE data from the analyzed zircons suggest their derivation mainly from the continental crustal type magmas but some grains, showing an overlap on the mafic fields (Fig. 5), do not rule out their derivation, at least partly, from the crystallization of oceanic crust (Hoskin, 2005; Grimes et al., 2015). Other trace elements also show distinct peaks for Pb, Th, U, and Hf, and troughs for Ba, Sr, Eu, and Nb (Fig. 5).

We also plotted trace element contents or ratios from the analyzed zircons on several discrimination diagrams presented in Hoskin (2005) and Grimes et al. (2015). The data mainly plot in the continental crustal fields (Fig. 6a–c), but several analyses stretch into mafic fields (Fig. 6c-d). These pieces of evidence suggest existence of some mafic component that was mixed with the felsic magma from which the zircons crystallized apart from its dominant portion which was likely derived from the continental crust. The data plot on the mantle zircon array on the Nb/Yb vs. U/Yb plot (Fig. 6e). On the U (ppm) vs. Th (ppm) diagram the data show a linear trend above the Th/U = 1 (Fig. 6f).

A bivariate plot of the total REE against LREE (Fig. 6g) displays a linear trend but data are indistinguishable from zircons of Gray and Pink granites. A linear trend between magmatic and hydrothermal origin on the $(Sm/La)_N$ vs. Ce/Ce* discrimination diagram of Hoskin (2005) was also observed for the analyzed zircons from both type granites (Fig. 6h). However, the prismatic crystal shapes, oscillatory zoning, and the linear trend among bivariate plots clearly indicate their igneous origin and may be indicating their formation during fractional crystallization from the granitic magma. We found no clear difference in the age data (the majority of the zircons U–Pb ages were concordant or nearly concordant with a peak around 750 Ma; Rehman et al., 2018) nor any significant variation in the Hf isotope compositions (described in the next section). Hence, the effect of hydrothermal event(s), if at all operative, was not significant to propose alternate interpretations. Moreover, the possibility of incorporation of the apatite, monazite, or xenotime inclusion (LREE enriched phases) during the laser ablation may have resulted in elevating the LREE values, and hence the trend may not be related to the hydrothermal activity. These pieces of evidence specify that the magmatism was mainly delimited within the Neoproterozoic times (750 to 640 Ma) however three zircon grains in the Pink granite (Sample NP10; spots #2, #4, and #9) returned younger U–Pb ages of 436 ± 12 Ma, 564 ± 13 Ma, and 421 ± 10 Ma, respectively, (Table 3) that may indicate Pb-loss or effect of secondary process. Titanium contents in the above three analysis were also anomalously high and the resulting temperatures were >900 °C (supplementary Table S1 and Fig. S2).

Titanium contents among the analyzed spots vary between 2 and 109 ppm in Gray granite sample NGP62a (except two analyses that have extremely higher Ti contents of 109 and 68 ppm, Table 2). Other samples also exhibit more or less similar values, with several spots yielding anomalously higher Ti contents which perhaps indicate the incorporation of Ti from the Ti-rich phases (rutile, ilmenite etc.) during the LA-ICP-MS analysis. Such abnormal Ti values (>50 ppm) were excluded from the temperature assessments. The analyzed spots show crystallization temperatures (based on the Ti-in-zircon thermometer after Watson et al., 2006) between 631 and 905 °C (Table 2 and see supplementary Table S1, available on-line). These values were relatively lower (up to 100 to 150 °C) than the values obtained from the zircon saturation temperatures (784 to 918 °C) but within the range of the commonly stated values for the crystallization of granitic melts (Pupin, 1980; Watson and Harrison, 1983; Hanchar and Watson, 2003; Miller et al., 2003; Fu et al., 2008). A recent research by Schiller and Finger (2019) raised the issue of the activity of TiO_2 and SiO_2 on the Ti-in-zircon thermometry during zircon crystallization in granitic rocks. Those authors stressed that the application of Ti-in-zircon thermometry needs upward correction of +70 °C relative to the original TiO_2 and SiO_2-saturated calibration of the thermometer introduced by Watson et al. (2006). Keeping this in view, we corrected the Ti-in-zircon thermometry-based results (supplementary Table S1 available on-line) and the newly obtained T values are in agreement with the Zr-saturation

temperatures from the whole-rock, showing a range between 663 and 975 °C, displaying slightly wider range. This is because the LA-ICP-MS spots size (30–40 μm) requires relatively larger spatial resolution and, therefore, has some limitations. Overall, if calibrated for the TiO_2 and SiO_2 activities, based on the observations of Schiller and Finger (2019), the temperature estimates might be within the geologically meaningful limits for the crystallization of granitic melts.

3.3. Hafnium isotope data of zircons

In-situ Hf isotope analysis, U–Pb age, and εHf (t) values for the analyzed spots from representative zircon grains are shown in Fig. 4. Hafnium concentrations of the analyzed spots in zircons from both granites are quite similar, ranging from 5000 to 14000 ppm, with a few exceptions of lower Hf contents (see detailed results in supplementary Table S1; available on-line). There was no systematic relationship between the Hf content (similar in case of other trace elements) and internal morphology or textural appearance of zircons. The $^{176}Hf/^{177}Hf$ ratios vary between 0.282504 and 0.282753 (average: 0.282608), and the εHf(t) values of zircons range from +5.7 to +14.4 in Gray granites and +1.9 to 10.7 in Pink granite. The relatively lower εHf(t) values from the same three spots discussed above (#2, #4, and #9) were calculated from the relatively younger and discordant U–Pb ages of 436, 564, and 421 Ma, respectively, none of them signify the Neoproterozoic magmatism, hence the εHf(t) values may not be meaningful. When the values were calculated with the 750 Ma (concordant age from the majority of NPIC zircons) the results from the three anomalous spots showed εHf(t) values of +10.0, +10.3, and +8.3, respectively, identical to the values obtained from the majority of the analyzed spots. The calculated T_{DM} model age (Table 3) for the analyzed zircons ranged from 736 to 1119 Ma for Gray granites and 900 to 1013 Ma for Pink granites, again yielding almost identical model age for the granite source material. The εHf (t) values against U–Pb age data plot on the crust-mantle evolution diagram above the Chondrite Uniform Reservoir (CHUR) line in the positive field (Fig. 7), suggesting a juvenile crust with no input of the ancient crust (Scherer et al., 2007). For comparison, we plotted εHf(t) values of zircons reported in past studies (e.g., NPIC: +8.2 to +14.0 in Mastoi et al., 2019; MIS: +0.5 to +9.5 in de Wall et al., 2018; Seychelles: +2.2 to +13.2 in Shellnutt et al., 2020), and the results are consistent with our data, showing a significant overlap and all lacking negative εHf(t) values, inferring a juvenile crust-derived source.

4. Interpretation of results

4.1. Implications from zircon trace element and Hf isotope geochemistry

The zircon trace element geochemistry and Hf isotope offer strong implications toward understanding the petrogenetic and magmatic source of the NPIC granites. Trace elements (including REE) data, and chondrite-normalized diagrams (Fig. 5) indicate derivation of the granitic magma from a continental crust through partial melting, followed by plagioclase fractionation (Eu anomaly), while some mafic component (oceanic crust) was also likely incorporated in the formation of zircons. Different discriminatory bivariate diagrams (Fig. 6) show an overlap of the zircon trace element contents in mafic and felsic fields. There is no clear correlation or trend from mafic to felsic or vice versa among the analyzed zircons, however, the similar Ce/Ce* values to the igneous zircons (Hoskin, 2005) and micro inclusions (apatite, monazite, xenotime, and plagioclase) direct towards the Si-saturated continental crustal magmas (Maas et al., 1992). Albeit minor mafic components (partial melting of the tonalitic-dioritic, and gabbroic basement rocks or assimilation of the above in the granitic magma) may not be ruled out from which some of the zircons were crystallized, the common textural and petrological features make it hard to distinguish those derived from mafic crust. Presence of the Eu anomaly in whole-rock data as well as in zircons attest to the fractional crystallization of magma.

In addition to the evidences learned from the zircon trace element geochemistry, Hf isotope geochemistry also supports the derivation of precursors of the NPIC granitoids solely from a juvenile crust. In our previous study (Rehman et al., 2018), we proposed possible assimilation of the country rocks by the uprising magma to produce the Pink granites, however indistinguishable Hf isotope values and comparable trace element geochemistry of zircons in both Gray and Pink granites rule out any contamination of the parental magma by the older preexisting crust. The highly radiogenic and positive εHf (t) values (+5 to +14) and 1100 to 736 Ma T_{DM} model ages from the analyzed zircons (Table 3 and Fig. 8) indicate the source material was primarily derived from a juvenile crust that underwent partial melting to produce granitoids. Absence of negative εHf (t) values advocate a lack of the reworked older continental crust in the formation of NPIC and other granitoids discussed in this study. The Ti-in-zircon temperatures (634 to 904 °C), oscillatory zoning, and equivalent ages from zircons in both granite types further approve their progressive crystallization mainly from the continental crustal source.

4.2. Petrogenetic source

The Neoproterozoic granitoids of the NPIC as well as those on the MIS, Madagascar, and Seychelles were interpreted as A-type, post-orogenic within-plate granitoids on the basis of whole-rock geochemistry (e.g., Crawford and Compston (1969); Dhar et al. (1996); Eby and Kochhar (1990); Jan et al. (1997, 2014, 2018); Torsvik et al. (2001a, 2001b); Ashwal et al. (2002, 2013); Sharma (2005); Khan et al. (2012, 2017); Meert et al. (2013); Kumar et al. (2020)). The whole-rock major and trace elements data, used from past publications, infer post-orogenic calc-alkaline and shoshonitic series, ferroan, A-type, peraluminous (predominant) to peralkaline granitoids that likely formed in extensional within-plate tectonic settings (Fig. 2). Our newly obtained trace element data from zircon, depicted by distinct negative Eu anomaly, Zr, Nb, and Ce enrichment, and Ba and Sr depletion (Fig. 5) provide strong evidence for the derivation of its magma from the partial melting of continental crust that was fractionating feldspar during the zircon crystallization (e.g. Pearce et al., 1984). The Ga/Al ratios in the studied granites typify A-type granites that likely generate in post-orogenic within-plate tectonic settings (Whalen et al., 1987; Eby, 1990, 1992; Eby and Kochhar, 1990; Ashwal et al., 2002). Moreover, whole-rock major and trace element compositions and emplacement ages of granites of the NPIC, MIS, Seychelles, Madagascar, and South China Block are alike (ca. 750 Ma). We assume these Neoproterozoic granitoids formed in a rift-related within-plate tectonic settings that are also supported by the paleomagnetic records reported from rocks of the above-mentioned areas (Li et al., 2008; Ashwal et al., 2013).

4.3. Regional relationship of NPIC granitoids with other Neoproterozoic granites

Paleoreconstruction of the MIS (NPIC as a part), Madagascar, Seychelles, and South China Block prior to the Neoproterozoic times indicate a single domain within the Rodinia supercontinent (Li et al., 2008). Subduction of the oceanic crust along the western margin of

Table 2
Trace element concentrations (in ppm) from the analyzed zircons of Gray granite (Sample NGP62a).

Element/Spot#	1	2	3	4	5	6	7	8	9	10	11	12	13	14	15
Si	149,581	149,581	149,581	149,581	149,581	149,581	149,581	149,581	149,581	149,581	149,581	149,581	149,581	149,581	149,581
P	697.16	1568.56	1493.66	937.09	977.55	1276.51	784.17	539.49	1182.51	657.78	661.35	794.07	1548.47	767.68	529.23
Ca	<114.00	3221.52	520.83	<101.63	<99.86	<113.37	<118.05	<113.87	<161.86	<131.20	<115.91	<102.24	679.10	127.29	<131.35
Ti	2.74	109.37	2.86	2.79	2.58	2.73	2.71	2.54	2.88	2.66	2.57	2.68	2.93	3.10	2.49
V	<0.154	0.61	<0.160	<0.140	<0.136	<0.153	<0.160	<0.153	<0.226	<0.185	<0.160	<0.144	<0.149	0.33	<0.188
Cr	<1.84	<2.50	<1.87	<1.70	<1.66	<1.86	<1.90	<1.91	6.98	<2.14	<1.88	<1.73	<1.78	<1.71	<2.08
Fe	<12.55	543.31	45.17	<12.06	<11.73	<12.65	179.32	<13.09	32.52	<15.02	<13.11	192.27	<12.92	24.08	<14.59
Sr	5.14	9.55	5.06	3.63	7.27	5.33	5.11	4.85	5.82	6.36	4.34	5.13	4.81	5.71	5.43
Y	3000	4274	2740	2012	4788	3256	2979	2826	3339	4364	2528	3117	2431	2579	3301
Nb	157.78	197.76	159.50	155.41	158.20	138.89	147.97	143.02	166.89	153.45	149.12	148.55	155.19	171.33	146.15
Ba	<0.66	1.90	<0.68	<0.62	<0.56	<0.66	<0.64	<0.64	<0.87	<0.77	<0.68	<0.64	<0.65	<0.65	<0.76
La	0.23	13.80	15.26	3.78	<0.069	4.68	0.30	<0.080	2.39	<0.090	0.20	0.40	22.83	0.84	0.43
Ce	22.30	62.10	63.55	32.64	31.08	38.04	25.14	16.60	40.74	24.97	21.02	22.52	100.63	27.58	21.77
Pr	0.30	6.54	6.82	1.46	0.17	2.31	0.29	0.28	0.74	0.31	0.31	0.33	10.64	0.57	0.55
Nd	3.86	24.51	37.36	9.26	4.68	15.01	4.39	5.83	5.62	7.99	3.83	4.57	51.51	3.84	8.43
Sm	8.80	16.21	17.29	5.82	14.47	13.50	10.14	12.92	6.93	17.45	9.23	11.05	18.94	7.15	12.97
Eu	1.20	1.84	1.48	0.78	1.77	0.99	1.38	1.62	0.77	2.45	1.03	1.37	1.43	0.88	1.66
Gd	63.43	78.22	64.25	36.62	100.29	71.61	64.28	72.77	50.22	104.63	52.74	67.47	58.03	45.32	86.51
Tb	22.85	32.04	20.90	12.94	37.53	24.71	22.85	24.47	20.74	35.95	18.30	23.80	18.58	17.37	28.30
Dy	280.74	399.26	248.35	165.00	466.78	305.57	278.76	282.23	276.75	425.01	222.83	290.87	224.73	227.94	328.25
Ho	101.48	146.40	89.80	63.20	168.27	110.76	101.65	98.86	106.62	153.98	82.63	104.45	80.31	83.00	114.01
Er	442.17	650.48	398.60	277.00	726.38	480.40	436.70	409.41	490.50	659.55	368.51	454.94	345.74	370.05	477.69
Tm	85.02	123.56	75.64	54.10	137.04	95.15	84.27	78.52	95.49	119.83	71.67	86.72	68.33	73.28	89.03
Yb	713.37	989.87	640.47	467.79	1133.27	816.58	713.32	655.64	792.82	960.22	608.06	737.08	580.18	622.08	733.40
Lu	113.68	164.17	107.56	77.92	168.71	131.16	112.11	104.10	137.49	162.39	105.46	117.72	91.07	97.56	122.78
Hf	7903	9378	7221	8023	7839	8930	7077	6169	8792	5971	6255	7776	7486	8206	5872
Pb^{206}	47.20	96.82	38.34	40.62	90.13	61.39	52.13	29.80	98.69	56.32	37.62	51.64	37.94	45.37	36.04
Pb^{207}	4.74	26.62	2.80	3.18	5.91	4.38	5.72	2.12	8.97	3.60	2.66	4.27	2.90	8.26	2.27
Pb^{208}	5.14	31.14	3.15	2.69	7.97	6.36	6.46	2.86	8.57	4.97	2.69	5.00	3.23	8.46	3.33
Th	57.78	113.22	41.19	37.93	117.33	83.86	58.35	38.35	94.85	74.49	37.28	62.57	38.54	64.42	46.87
U	99.27	172.49	79.06	85.49	187.71	123.44	99.65	61.24	191.98	114.02	73.13	105.97	76.79	95.89	68.76
Th/U	0.58	0.66	0.52	0.44	0.63	0.68	0.59	0.63	0.49	0.65	0.51	0.59	0.50	0.67	0.68
Ti-in-Zrn Temp	***639***		***642***	***640***	***635***	***638***	***638***	***633***	***642***	***637***	***634***	***637***	***643***	***648***	***632***
Ti-in-Zrn cor T (°C)	**709**		**712**	**710**	**705**	**708**	**708**	**703**	**712**	**707**	**704**	**707**	**713**	**718**	**702**
(Sm/La)N	62.63	1.88	1.81	2.47		4.62	53.77		4.64		73.90	44.68	1.33	13.66	47.86
Ce/Yb	0.03	0.06	0.10	0.07	0.03	0.05	0.04	0.03	0.05	0.03	0.03	0.03	0.17	0.04	0.03
U/Yb	0.14	0.17	0.12	0.18	0.17	0.15	0.14	0.09	0.24	0.12	0.12	0.14	0.13	0.15	0.09
Nb/Yb	0.22	0.20	0.25	0.33	0.14	0.17	0.21	0.22	0.21	0.16	0.25	0.20	0.27	0.28	0.20
Gd/Yb	0.09	0.08	0.10	0.08	0.09	0.09	0.09	0.11	0.06	0.11	0.09	0.09	0.10	0.07	0.12
U/Nb	0.63	0.87	0.50	0.55	1.19	0.89	0.67	0.43	1.15	0.74	0.49	0.71	0.49	0.56	0.47
Th/Yb	0.08	0.11	0.06	0.08	0.10	0.10	0.08	0.06	0.12	0.08	0.06	0.08	0.07	0.10	0.06
Eu/Eu*	0.16	0.16	0.14	0.16	0.14	0.10	0.16	0.16	0.13	0.17	0.14	0.15	0.13	0.15	0.15
Ce/Ce*	33.56	2.54	2.42	5.42		4.51	33.28		11.91		33.06	24.24	2.51	15.53	17.31
ΣREE	1859	2709	1787	1208	2990	2110	1856	1763	2028	2675	1566	1923	1673	1577	2026
LREE (La-Eu)	37	125	142	54	52	75	42	37	57	53	36	40	206	41	46
HREE (Gd-Lu)	1823	2584	1646	1155	2938	2036	1814	1726	1971	2622	1530	1883	1467	1537	1980
LREE/HREE	0.02	0.05	0.09	0.05	0.02	0.04	0.02	0.02	0.03	0.02	0.02	0.02	0.14	0.03	0.02

Footnote to Table 2. Ti-in-zircon temperatures are calculated after Watson et al. (2006). Ti-in-Zrn cor T (°C) mean the temperatures values are corrected (+70 °C) after the observations of Schiller and Finger (2020).

Rodinia facilitated to produce the heat source that partially melted the overriding continental lithosphere to generate granitic magma that ultimately formed the MIS (including NPIC), Madagascar, Seychelles, and the South China Block granitoids. Past researchers (e.g. Torsvik et al., 2001b; Dharma et al., 2012; Ashwal et al., 2013) proposed that granites of the MIS and Seychelles formed from the subduction-related magmatism in an Andean-type arc setting. The slightly older basement to the NPIC granites was also inferred by Jan et al. (2018) to have been formed in a similar tectonic setting. Based on extensive U–Pb data of zircon, Rehman et al. (2018) interpreted a prolonged magmatism (>100 million years) to produce the NPIC granitoids and associated MIS rocks and the initiation of magmatism was triggered by the subduction of the Mozambique Ocean (Meert et al., 2013) which later shifted to rift-related tectonic setting above a plume (Li et al., 2008 and references therein).

The discussion above provides sufficient pieces of evidence for genesis of the parent magma that likely initiated from the partial melting of the eastward subducting Mozambique oceanic crust and the subsequent melting of continental crust and within-plate rift-related magmatism generated the Neoproterozoic granitoids. Wang et al. (2017) compared Hf isotope data of the zircons collected from the Neoproterozoic granitoids of the South China Block with those of MIS, and interpreted that the two blocks (also Seychelles and Madagascar) remained juxtaposed along the periphery of Rodinia and coincide with the breakup of the supercontinent. Zircon geochemistry from this study and those reported in past publications confirm a bimodal magmatism,

16	17	18	19	20	21	22	23	24	25	26	27	28	29	30
149,581	149,581	149,581	149,581	149,581	149,581	149,581	149,581	149,581	149,581	149,581	149,581	149,581	149,581	149,581
743.80	38283.13	436.81	959.04	466.83	502.56	1877.28	1763.85	382.74	529.11	314.36	352.62	479.17	454.89	600.59
<132.85	9753.80	<155.77	<272.14	<102.21	<103.70	1402.36	1549.71	<104.31	<98.18	<119.63	<114.19	<97.40	<115.62	<261.84
3.08	68.43	2.80	5.35	2.98	2.77	3.63	3.59	2.52	2.47	2.67	2.71	2.90	2.75	8.61
<0.185	9.82	<0.227	0.53	<0.137	<0.144	0.33	<0.134	<0.150	<0.137	<0.174	<0.160	0.18	<0.159	<0.36
<2.11	<2.22	<2.29	27.28	<1.48	<1.59	<1.84	<1.52	<1.61	<1.53	<1.82	<1.69	<1.47	<1.76	10.77
33.41	27045.31	<16.13	147.61	<10.08	21.50	138.16	158.04	<9.86	<9.38	<11.17	<10.04	<8.82	54.24	599.97
4.04	595.31	5.09	13.56	5.03	5.50	8.60	9.55	4.94	6.37	5.13	4.05	6.89	3.85	10.02
2198	67,974	2740	5062	2651	3067	4699	5392	3016	4026	3192	2513	4478	2107	4915
146.60	419.15	149.48	192.03	162.52	152.59	188.97	181.19	142.49	148.04	141.72	135.53	150.99	150.88	192.59
<0.75	585.10	<0.88	5.90	<0.58	<0.62	<0.70	<0.59	<0.60	<0.56	<0.66	<0.63	<0.54	<0.68	<1.54
8.76	46.97	0.91	8.61	0.32	0.37	62.23	88.38	<0.073	<0.069	<0.085	<0.082	2.27	1.18	17.89
42.39	487.89	26.75	60.07	30.78	21.45	248.17	340.28	19.62	29.09	16.36	27.22	30.10	27.35	89.47
3.94	57.05	0.46	3.82	0.27	0.39	29.51	41.79	0.09	0.17	0.36	0.16	0.19	0.60	3.79
20.82	352.01	2.75	19.32	2.84	4.77	154.90	218.74	3.21	3.91	7.63	3.92	3.54	4.84	18.08
11.33	385.95	6.59	17.96	6.59	11.30	54.14	75.55	11.17	12.55	15.70	10.72	13.14	6.78	14.36
0.88	38.46	0.84	1.62	0.86	1.41	3.40	4.82	1.38	1.23	1.80	1.14	1.76	0.77	1.19
43.44	1422.89	48.10	79.51	44.92	65.63	126.12	161.41	65.36	81.81	87.46	59.08	86.91	40.24	80.23
15.21	702.30	18.80	34.30	17.78	23.56	39.15	48.04	23.86	31.38	28.34	20.29	33.92	14.80	34.25
184.93	9610.11	238.39	464.64	229.57	284.88	453.49	544.06	283.54	388.69	322.17	237.17	421.27	183.40	449.28
70.03	3282.84	89.21	173.04	84.82	103.89	162.69	188.30	103.22	143.94	111.82	84.75	157.99	66.40	167.81
317.33	13702.28	393.42	786.02	377.48	442.07	703.18	809.85	447.10	617.97	466.60	357.76	700.46	293.01	763.12
62.41	2379.40	75.70	153.70	77.87	87.28	136.77	158.16	88.42	124.83	88.13	69.04	141.46	57.05	148.59
528.93	15790.33	617.77	1196.33	666.41	732.14	1129.13	1330.53	768.41	1078.01	748.66	601.93	1171.92	484.48	1193.87
93.50	1832.09	104.36	190.01	99.71	109.90	169.90	192.81	114.67	154.00	119.53	95.00	169.10	77.69	185.10
7291	7626	7355	9058	8388	7951	8087	7619	7655	8110	5814	5888	8705	7389	8801
42.22	590.03	46.54	90.77	55.19	45.95	194.59	158.04	56.52	90.02	32.21	33.95	96.63	39.45	144.38
5.23	278.83	6.90	19.80	4.64	4.89	16.55	13.79	4.03	6.33	2.10	2.34	7.16	3.13	20.42
4.83	302.61	6.90	28.47	4.82	5.43	18.97	14.24	5.24	7.74	3.06	2.72	8.65	3.18	19.11
35.18	3441.01	49.29	136.31	57.84	57.83	234.38	164.80	63.52	109.58	42.15	36.77	120.87	41.07	147.15
76.06	3697.18	85.10	207.43	123.19	97.36	396.62	326.42	114.72	191.48	63.65	68.07	211.76	78.70	302.81
0.46	0.93	0.58	0.66	0.47	0.59	0.59	0.50	0.55	0.57	0.66	0.54	0.57	0.52	0.49
647		***640***	***689***	***645***	***639***	***659***	***658***	***633***	***631***	***637***	***638***	***643***	***639***	***728***
717		**710**	**759**	**715**	**709**	**729**	**728**	**703**	**701**	**707**	**708**	**713**	**709**	**798**
2.07	13.16	11.58	3.34	33.19	48.64	1.39	1.37					9.27	9.20	1.29
0.08	0.03	0.04	0.05	0.05	0.03	0.22	0.26	0.03	0.03	0.02	0.05	0.03	0.06	0.07
0.14	0.23	0.14	0.17	0.18	0.13	0.35	0.25	0.15	0.18	0.09	0.11	0.18	0.16	0.25
0.28	0.03	0.24	0.16	0.24	0.21	0.17	0.14	0.19	0.14	0.19	0.23	0.13	0.31	0.16
0.08	0.09	0.08	0.07	0.07	0.09	0.11	0.12	0.09	0.08	0.12	0.10	0.07	0.08	0.07
0.52	8.82	0.57	1.08	0.76	0.64	2.10	1.80	0.81	1.29	0.45	0.50	1.40	0.52	1.57
0.07	0.22	0.08	0.11	0.09	0.08	0.21	0.12	0.08	0.10	0.06	0.06	0.10	0.08	0.12
0.12	0.16	0.14	0.13	0.15	0.16	0.13	0.13	0.16	0.12	0.15	0.14	0.16	0.14	0.11
2.81	3.67	16.17	4.08	41.10	21.83	2.25	2.18					18.07	12.69	4.23
1404	50,091	1624	3189	1640	1889	3473	4203	1930	2668	2015	1568	2934	1259	3167
88	1368	38	111	42	40	552	770	35	47	42	43	51	42	145
1316	48,722	1586	3078	1599	1849	2920	3433	1895	2621	1973	1525	2883	1217	3022
0.07	0.03	0.02	0.04	0.03	0.02	0.19	0.22	0.02	0.02	0.02	0.03	0.02	0.03	0.05

initiated from subduction-related mafic source leading to the rift- and plume-related within-plate felsic source.

Here, we present a schematic model showing the developmental stages and tectonic settings of the NPIC, MIS, and other Neoproterozoic granitoids of the Rodinia supercontinent (Fig. 8). It envisages, prior to 750 Ma, an Andean-type subduction of the Mozambique Ocean around the periphery of Rodinia (Ashwal et al., 2013; Meert et al., 2013; Wang et al., 2017; Cawood et al., 2018). The subduction likely caused the melting to generate magma beneath the overlying continental lithosphere that resulted in the formation of some of the structurally older mafic to andesitic basement (early-formed plutons) and rhyolites (Fig. 8a) Around 750 Ma, the magmatism reached to its peak when rifting occurred in the Rodinia supercontinent forming the dominant granitic plutons (Fig. 8b). Paleoreconstruction model show the Neoproterozoic plutons and rift-related volcanics of NPIC, MIS, Seychelles, Madagascar, and the South China Block in an arc-shaped Neoproterozoic domain, indicating traces of a former subduction (the Mozambique ocean) trailed by the rift to break-up the Rodinia (Fig. 8c).

5. Conclusions

1. Trace element geochemistry, in-situ Hf isotope ratios, and age data of zircons from Gray and Pink granites of the NPIC exhibit more or less matching geochemical features to those reported from granites of

Table 3
Hf isotope data of the NPIC zircons.

Sample	Spot#	t (Ma)	1σ	$^{176}Yb/^{177}Hf$	1σ	$^{176}Lu/^{177}Hf$	1σ	$^{176}Hf/^{177}Hf$	1σ	εHf(0)	εHf(t)	1σ	T_{DM}
Zircon from gray granites													
NGP62a_2	2	698	27	7.70641E−02	1.0E−03	2.46735E−03	5.3E−05	2.82642E−01	2.9E−05	−4.6	9.7	0.5	899
NGP62a_3	3	739	19	5.08158E−02	7.9E−04	1.70062E−03	1.9E−05	2.82605E−01	1.5E−05	−5.9	9.6	0.3	933
NGP62a_4	4	748	19	6.41466E−02	5.8E−04	2.06867E−03	6.5E−06	2.82561E−01	2.7E−05	−7.5	8.0	0.5	1006
NGP62a_6	6	754	19	7.48098E−02	2.4E−03	2.48709E−03	8.3E−05	2.82565E−01	1.8E−05	−7.3	8.1	0.3	1012
NGP62a_7	7	773	21	8.30028E−02	8.1E−04	2.57490E−03	5.2E−05	2.82542E−01	1.9E−05	−8.1	7.6	0.3	1048
NGP62a_8	8	738	19	7.33569E−02	2.4E−03	2.47284E−03	5.9E−05	2.82753E−01	2.8E−05	−0.7	14.4	0.5	736
NGP62a_9	9	750	20	5.38119E−02	2.4E−04	1.80687E−03	1.0E−05	2.82610E−01	2.0E−05	−5.7	9.9	0.4	929
NGP62a_10	10	732	18	8.87841E−02	2.8E−03	2.92866E−03	6.7E−05	2.82612E−01	2.0E−05	−5.7	9.1	0.4	955
NGP62a_12	12	749	20	7.67888E−02	1.7E−03	2.44680E−03	2.4E−05	2.82609E−01	2.0E−05	−5.8	9.6	0.4	947
NGP62a_13	13	747	21	5.21329E−02	8.9E−04	1.63514E−03	2.8E−05	2.82504E−01	2.1E−05	−9.5	6.2	0.4	1076
NGP62a_14	14	643	27	6.30940E−02	1.2E−03	2.05694E−03	1.8E−05	2.82619E−01	2.2E−05	−5.4	7.9	0.4	922
NGP62a_15	15	740	19	7.77784E−02	1.7E−03	2.60252E−03	5.0E−05	2.82576E−01	2.0E−05	−6.9	8.1	0.4	999
NGP62a_16	16	743	21	8.11977E−02	8.3E−04	2.62307E−03	5.2E−06	2.82640E−01	1.7E−05	−4.7	10.5	0.3	906
NGP62a_18	18	747	20	6.57974E−02	2.7E−04	2.15915E−03	1.1E−05	2.82630E−01	2.3E−05	−5.0	10.4	0.4	909
NGP62a_21	21	758	19	8.00354E−02	1.7E−03	2.41929E−03	4.8E−05	2.82638E−01	1.7E−05	−4.7	10.8	0.3	903
NGP62a_23	23	760	20	9.28026E−02	3.9E−03	2.97241E−03	1.3E−04	2.82594E−01	1.5E−05	−6.3	9.0	0.3	983
NGP62a_27	27	762	20	5.51369E−02	2.7E−03	1.83563E−03	9.4E−05	2.82647E−01	2.9E−05	−4.4	11.5	0.5	876
NGP62b_5	5	742	17	8.22055E−02	5.5E−04	2.61924E−03	3.0E−05	2.82520E−01	2.5E−05	−8.9	6.2	0.4	1082
NGP62b_6	6	731	17	8.81739E−02	6.9E−04	2.93680E−03	3.9E−05	2.82676E−01	1.7E−05	−3.4	11.3	0.3	860
NGP62b_7	7	707	21	7.22840E−02	2.6E−04	2.46998E−03	4.9E−06	2.82692E−01	2.7E−05	−2.8	11.6	0.5	825
NGP62b_13	13	739	18	9.30188E−02	7.1E−03	3.02751E−03	2.2E−04	2.82651E−01	2.7E−05	−4.3	10.6	0.5	899
NGP62b_15	15	678	18	9.51201E−02	1.1E−02	3.03596E−03	3.0E−04	2.82599E−01	2.0E−05	−6.1	7.5	0.4	977
NGP62b_16	16	679	21	5.74598E−02	2.1E−03	1.84469E−03	7.9E−05	2.82588E−01	2.5E−05	−6.5	7.7	0.4	961
NGP62b_17	17	717	18	5.40535E−02	1.3E−03	1.77261E−03	2.4E−05	2.82621E−01	2.6E−05	−5.3	9.7	0.5	912
NGP62b_19	19	768	19	4.86171E−02	8.0E−04	1.62398E−03	3.1E−05	2.82624E−01	2.3E−05	−5.2	10.9	0.4	904
NGP62b_20	20	713	17	6.43030E−02	8.5E−04	2.14810E−03	2.9E−05	2.82595E−01	3.0E−05	−6.3	8.5	0.5	959
NGP62b_28	28	717	18	8.19206E−02	6.5E−04	2.74945E−03	2.0E−05	2.82595E−01	2.1E−05	−6.3	8.3	0.4	975
NGP62b_30	30	752	18	7.84016E−02	2.0E−03	2.59408E−03	4.8E−05	2.82638E−01	1.9E−05	−4.7	10.6	0.3	908
NGP62b_33	33	749	17	7.36464E−02	1.3E−03	2.41506E−03	3.0E−05	2.82625E−01	1.7E−05	−5.2	10.1	0.3	922
NGP62b_35	35	715	18	9.91272E−02	6.1E−03	3.23343E−03	2.4E−04	2.82715E−01	2.7E−05	−2.0	12.2	0.5	809
NP01_01	1	771	19	9.13009E−02	2.5E−03	3.34416E−03	8.3E−05	2.82618E−01	2.3E−05	−5.4	9.9	0.4	957
NP01_04	4	704	16	6.55881E−02	9.4E−04	2.37291E−03	2.2E−05	2.82607E−01	2.1E−05	−5.8	8.6	0.4	948
NP01_05	5	693	16	7.57335E−02	4.3E−04	2.82377E−03	2.1E−05	2.82587E−01	2.8E−05	−6.5	7.5	0.5	989
NP01_14	14	752	17	7.38624E−02	3.2E−03	2.61770E−03	1.1E−04	2.82574E−01	2.8E−05	−7.0	8.3	0.5	1002
NP01_14a	14a	752	17	6.05948E−02	1.5E−03	2.25977E−03	4.6E−05	2.82574E−01	1.8E−05	−7.0	8.5	0.3	993
NP01_15	16	758	19	9.51001E−02	7.2E−04	3.35398E−03	1.5E−05	2.82654E−01	2.5E−05	−4.2	10.9	0.4	903
NP01_22	22	772	18	6.70143E−02	2.0E−03	2.35790E−03	5.3E−05	2.82588E−01	1.7E−05	−6.5	9.3	0.3	975
NP01_24	24	800	19	8.04384E−02	6.3E−04	2.79187E−03	1.4E−05	2.82620E−01	2.8E−05	−5.4	10.8	0.5	939
NP01_25	25	754	18	9.21704E−02	8.3E−04	3.40246E−03	3.1E−05	2.82511E−01	2.9E−05	−9.2	5.7	0.5	1119
NP01_30	30	680	17	7.55446E−02	7.2E−04	2.79371E−03	1.6E−05	2.82609E−01	2.6E−05	−5.8	8.0	0.5	956
NP01_42	42	772	20	6.22762E−02	5.0E−04	2.23530E−03	1.7E−05	2.82577E−01	2.9E−05	−6.9	9.0	0.5	988
NP62_01	1	704	17	9.23264E−02	2.1E−03	3.07978E−03	6.2E−05	2.82560E−01	2.5E−05	−7.5	6.6	0.4	1036
NP62_02	2	736	19	8.30641E−02	4.6E−04	2.68962E−03	1.9E−05	2.82643E−01	2.9E−05	−4.6	10.4	0.5	903
NP62_14	14	744	20	7.90554E−02	1.9E−03	2.55826E−03	6.0E−05	2.82634E−01	2.0E−05	−4.9	10.3	0.4	913
NP62_16	16	782	19	6.96319E−02	9.5E−04	2.28445E−03	3.1E−05	2.82593E−01	2.6E−05	−6.3	9.8	0.5	966
NP62_17	17	758	19	7.16095E−02	2.3E−03	2.37643E−03	7.2E−05	2.82559E−01	2.1E−05	−7.5	8.0	0.4	1018
NP62_18	18	745	20	7.29514E−02	7.4E−04	2.40870E−03	2.3E−05	2.82568E−01	2.5E−05	−7.2	8.1	0.4	1005
NP62_24	24	834	24	8.59189E−02	1.3E−03	2.87974E−03	4.1E−05	2.82624E−01	1.9E−05	−5.2	11.6	0.3	936
NP62_25	25	747	20	5.33744E−02	6.2E−04	1.76910E−03	2.2E−05	2.82607E−01	2.0E−05	−5.8	9.8	0.4	932
NP62_31	31	675	19	6.84042E−02	5.5E−04	2.27332E−03	1.5E−05	2.82617E−01	2.7E−05	−5.5	8.4	0.5	930
NP62_35	35	722	19	5.54343E−02	7.7E−04	1.77451E−03	1.8E−05	2.82596E−01	2.8E−05	−6.2	8.9	0.5	948
NP62_36	36	724	18	6.72374E−02	2.2E−03	2.13731E−03	6.3E−05	2.82690E−01	2.0E−05	−2.9	12.1	0.4	821
NP62_38	38	712	19	8.13480E−02	3.6E−03	2.38891E−03	8.7E−05	2.82640E−01	2.8E−05	−4.7	9.9	0.5	900
NP62_39	39	710	21	9.47252E−02	2.2E−03	2.86056E−03	7.4E−05	2.82607E−01	1.5E−05	−5.8	8.5	0.3	960
NP62_40	40	770	20	8.20150E−02	2.2E−03	2.56792E−03	5.4E−05	2.82668E−01	2.2E−05	−3.7	12.0	0.4	863
Zircon from pink granites													
NP10_02	2	436	12	9.83616E−02	2.4E−03	3.02514E−03	8.3E−05	2.82629E−01	2.2E−05	−5.1	3.7	0.4	932
NP10_04	4	564	13	6.53020E−02	1.1E−03	2.16365E−03	1.7E−05	2.82624E−01	2.1E−05	−5.2	6.4	0.4	917
NP10_09	9	421	10	1.24431E−01	7.3E−03	4.25772E−03	2.7E−04	2.82598E−01	3.0E−05	−6.2	1.9	0.5	1013
NP10_12	12	741	17	1.24752E−01	4.2E−03	4.10413E−03	1.8E−04	2.82669E−01	2.7E−05	−3.6	10.7	0.5	900
NP10_13	13	704	16	1.10510E−01	1.4E−03	3.63496E−03	4.0E−05	2.82617E−01	2.9E−05	−5.5	8.4	0.5	966

t (Ma)

$\varepsilon Hf(0) = 10000*\{[(176Hf/177Hf)_{s(0)}/(176Hf/177Hf)_{CHUR(0)} - 1\}$

$\varepsilon Hf(t) = 10000*\{[(176Hf/177Hf)_{s(0)} - (176Lu/177Hf)_{s(0)}*(e^{\lambda*t*10^{-6}} - 1)]/[(176Hf/177Hf)_{CHUR(0)} - (176Lu/177Hf)_{CHUR(0)}*(e^{\lambda*t*10^{-6}} - 1)] - 1\}$

$\lambda = \lambda_{176} = 1.867*10^{(-11)}$ (/yr, by Söderlund et al., 2004)

$(176Hf/177Hf)_{CHUR(0)} = 0.282772$ (By Blichert-Toft and Albarède, 1997)

$(176Lu/177Hf)_{CHUR(0)} = 0.0332$ (By Blichert-Toft and Albarède, 1997)

$T_{DM} = 1/\lambda*\ln[1+(176Hf/177Hf_{sample(0)} - 176Hf/177Hf_{DM(0)})/(176Lu/177Hf_{sample(0)} - 176Lu/177Hf_{DM(0)})]$

$176Hf/177Hf_{DM(0)} = 0.28325$ (By Griffin et al., 2000)

$176Lu/177Hf_{DM(0)} = 0.0384$ (By Griffin et al., 2000)

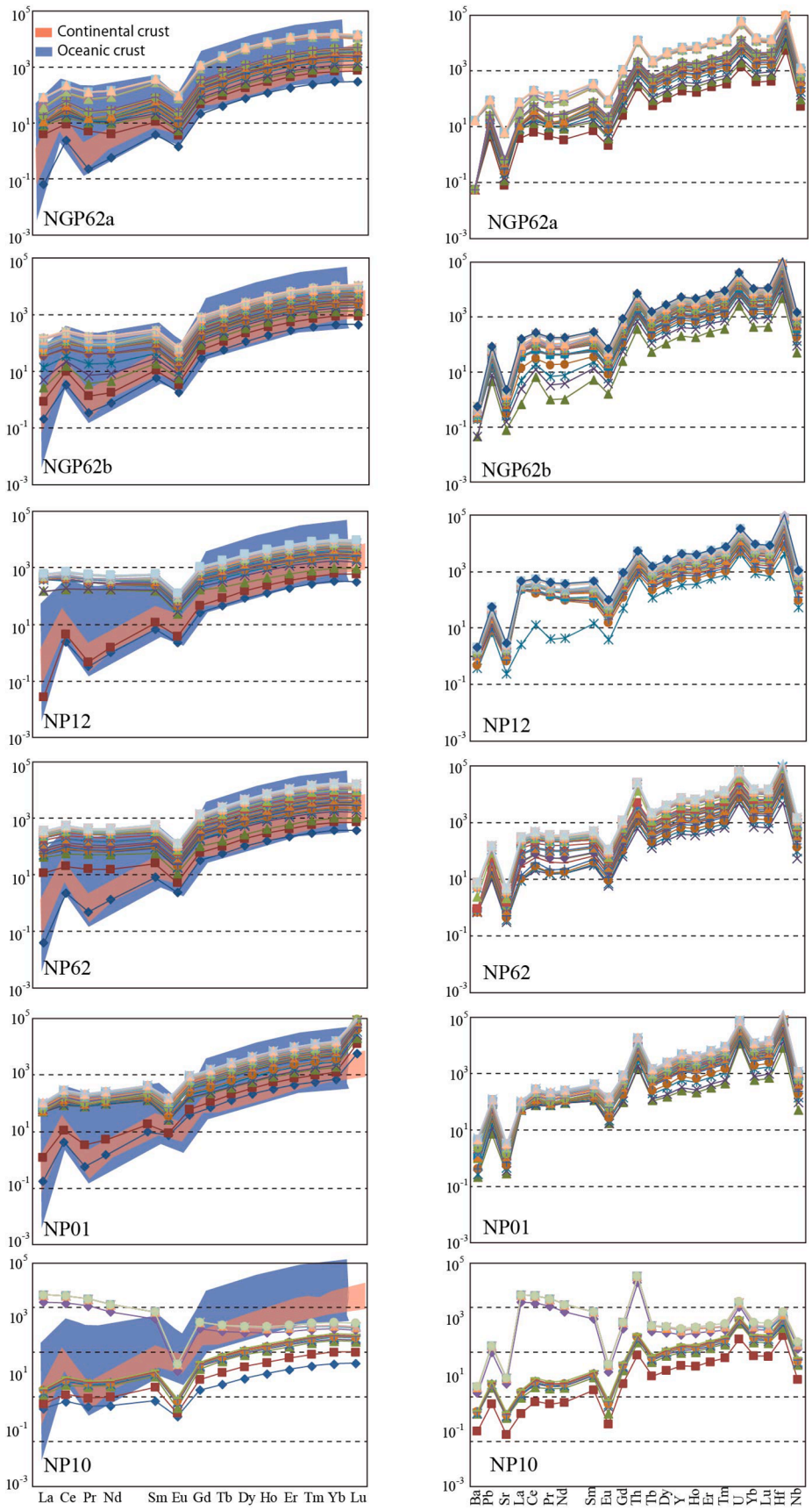

Fig. 5. Chondrite-normalized REE and trace-element data (McDonough and Sun, 1995) for the analyzed zircons from the NPIC granites. Fields for the continental zircons are after Hoskin and Ireland (2000) and for the ocean crust zircons after Grimes et al. (2007).

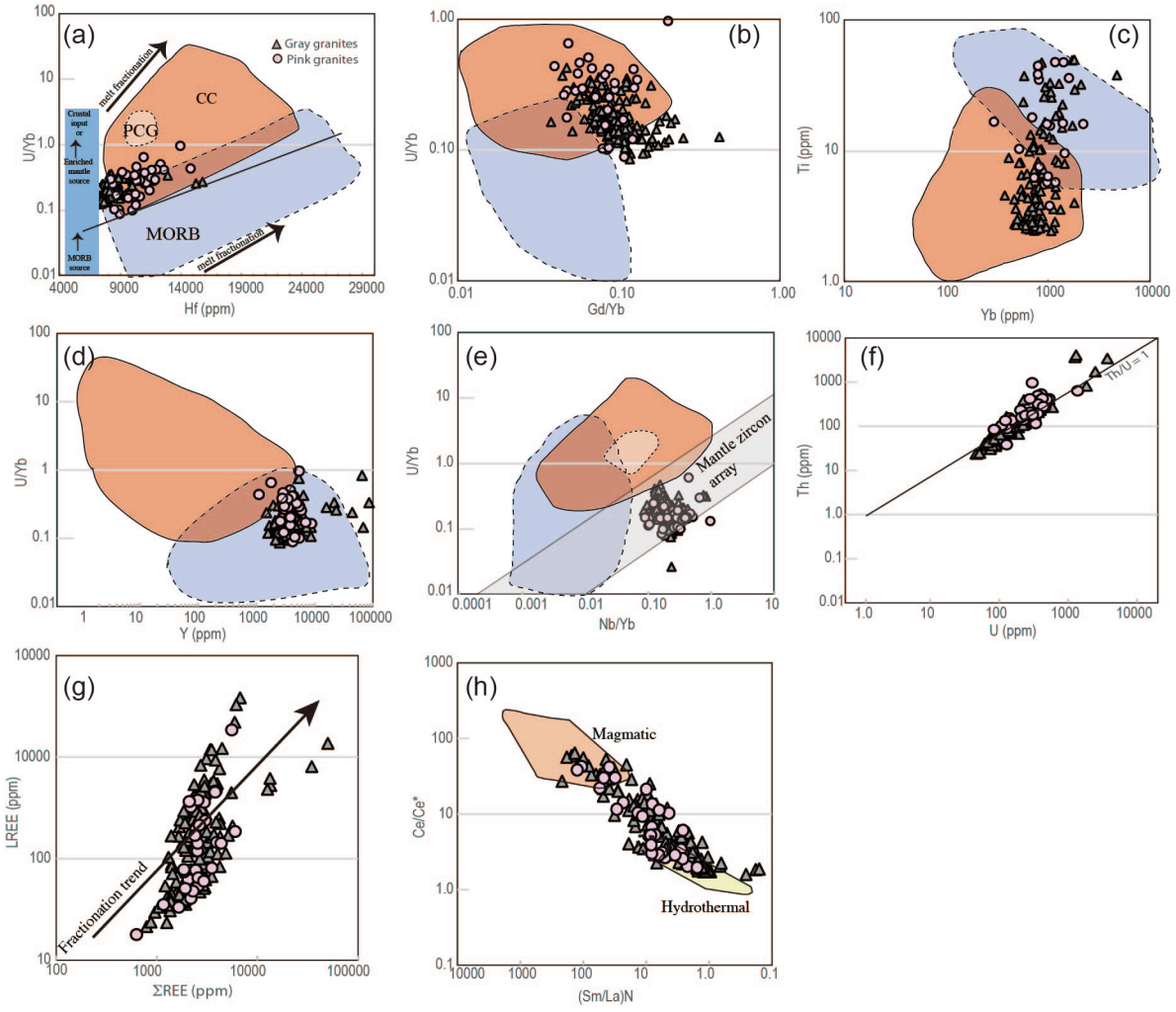

Fig. 6. Trace element data of zircons from the NPIC granitoids plotted on binary discrimination diagrams of Hoskin (2005), Grimes et al. (2007) and Grimes et al. (2015). (a) Hf (ppm) vs. U/Yb, (b) Gd/Yb vs. U/Yb, (c) Yb (ppm) vs. Ti (ppm), (d) Y (ppm) vs. U/Yb, (e) Nb/Yb vs. U/Yb, (f) U (ppm) vs. Th (ppm), (g) total REE (ppm) vs. LREE (ppm), and (h) $(Sm/La)_N$ vs. Ce/Ce*. Data from Gray and Pink granites predominantly plot in the continental arc granitoids field, indicating indistinguishable magma source for both granite types. However, some data show a tendency towards mafic fields, suggesting the presence of mafic component (calc-alkaline arc-related magmatism). Fields for continental arc granitoids (CC), post-collisional granitoids (PCG), and Mid-Ocean-Ridge-Basalt (MORB) are after Grimes et al. (2015) and for magmatic and hydrothermal zircons after Hoskin (2005). (For interpretation of the references to colour in this figure legend, the reader is referred to the web version of this article.)

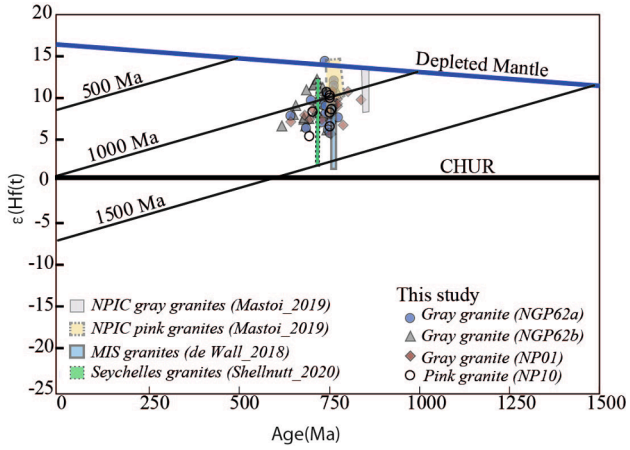

Fig. 7. Plot demonstrating the εHf(t) versus age of the NPIC Gray and Pink granites. Data from the past publications (NPIC zircons by Mastoi et al., 2019; MIS zircons by de Wall et al., 2018; and Seychelles zircons by Shellnutt et al., 2020) shown for comparison. The positive εHf(t) values, plot above the Chondrite Uniform Reservoir (CHUR), indicate a juvenile crust with no signs of the ancient crust. (For interpretation of the references to colour in this figure legend, the reader is referred to the web version of this article.)

MIS, Madagascar, Seychelles, and South China Block, suggesting a common petrogenetic source under similar tectonic settings.

2. Trace element (including REE) compositions, exhibited by the positive slope from La to Lu, positive Ce- and negative Eu-anomaly indicate the studied zircons formed from magma that was fractionating plagioclase during emplacement. Comparatively variable Ce/Ce* ratios, smaller Eu/Eu* anomalies, and high Th/U ratios (>0.30) point towards zircon derivation from continental crust.
3. The zircon saturation temperatures (784 to 918 °C) and the Ti-in-zircon corrected thermometry (663 to 975 °C) data are consistent with the temperature ranges commonly reported for granite crystallization.
4. The positive εHf(t) values of zircons in both Gray and Pink granites indicate juvenile crust with no involvement of the reworked ancient continental crust. The almost identical and young T_{DM} model ages (1119 to 736 Ma) further confirm the above assertion.
5. Petrological, mineralogical, and geochemical similarities (including Hf isotope data) of granitoids from the NPIC, MIS, Madagascar, Seychelles, and South China Block, and their paleo-tectonic setting make it clear that these granitoids were formed, dominantly, in a rift-related tectonic setting along the western margin of Rodinia supercontinent, however, calc-alkaline arc-related magmatism may have initiated due to the eastward subduction of the Mozambique Ocean before the peak magmatic event.

CRediT authorship contribution statement

Hafiz Ur Rehman: Conceptualization, Methodology, Investigation, Visualization, Software. **Tahseenullah Khan:** Methodology, Investigation. **Hao-Yang Lee:** Methodology, Software. **Sun-Lin Chung:** Methodology, Supervision, Validation. **M. Qasim Jan:** Investigation, Conceptualization. **Tehseen Zafar:** Methodology. **Mamoru Murata:** Methodology, Conceptualization.

Declaration of Competing Interest

The authors declare that they have no known competing financial interests or personal relationships that could have appeared to influence the work reported in this paper.

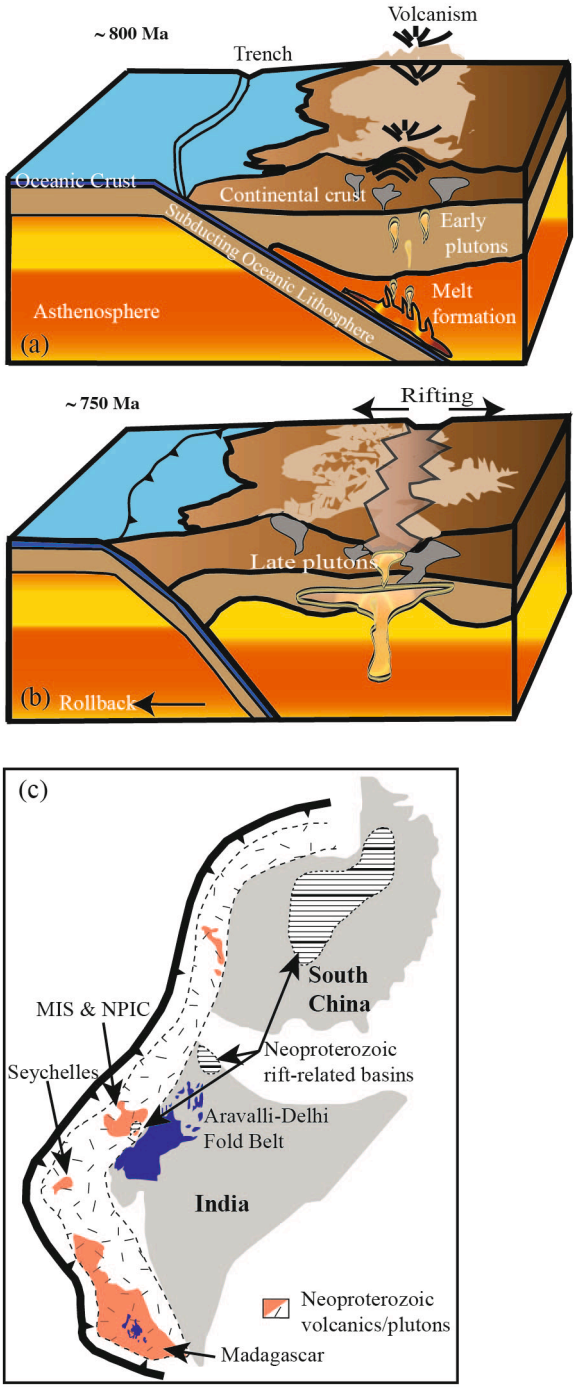

Fig. 8. Schematic tectonic model for the subduction and rifting in the Rodinia Supercontinent during the Neoproterozoic era. (a) Stage showing the subduction of the oceanic lithosphere prior to 750 Ma that initiated magmatism along the western periphery of Rodinia, (b) stage exhibited by rift-related within-plate magmatism forming the dominant granitic plutons of NPIC, MIS, Madagascar, Seychelles, and South China Block, (c) plate reconstruction during the Neoproterozoic era where a subduction zone (Mozambique Ocean) along the western margin of Rodinia triggered partial melting of the continental crust to produce granitoids of NPIC/MIS, Madagascar, Seychelles, and South China Block. Figure not to scale and sketched after the information from the past publications (Li et al., 2008; Ashwal et al., 2013; Meert et al., 2013; Wang et al., 2017; Cawood et al., 2018).

Acknowledgements

Due thanks to Chien-Hui Hung, Jui-Ting Tang, Yu-Han Chang and Shu-Yen Chen for their help in the analysis. This work was partly supported by the JSPS Kakenhi fund (#15K05316 to HUR) and partly from the Taiwan MOST fund (# 1050021585 to SLC). MQJ thanks the Pakistan Academy for support.

Appendix A. Supplementary data

Supplementary data to this article can be found online at https://doi.org/10.1016/j.precamres.2020.106047.

References

Ashwal, L.D., Demaiffe, D., Torsvik, T.H., 2002. Petrogenesis of Neoproterozoic granitoids and related rocks from the Seychelles: the case for an Andean-type arc origin. J. Petrol. 43, 45–83.
Ashwal, L.D., Solanki, A.M., Pandit, M.K., Corfu, F., Hendriks, B.W.H., Burke, K., Torsvik, T.H., 2013. Geochronology and geochemistry of Neoproterozoic Mt. Abu granitoids, NW India: Regional correlation and implications for Rodinia paleogeography. Precambr. Res. 236, 265–281.
Belousova, E., Griffin, W., O'Reilly, S.Y., Fisher, N., 2002. Igneous zircon: trace element composition as an indicator of source rock type. Contrib. Miner. Petrol. 143 (5), 602–622.
Belousova, E.A., Griffin, W.L., O'Reilly, S.Y., 2006. Zircon crystal morphology, trace element signatures and Hf isotope composition as a tool for petrogenetic modeling: examples from Eastern Australian granitoids. J. Petrol. 47, 329–353.
Blichert-Toft, J., Albarède, F., 1997. The Lu–Hf isotope geochemistry of chondrites and the evolution of the mantle–crust system. Earth Planet. Sci. Lett. 148 (1-2), 243–258.
Cawood, P.A., Zhao, G., Yao, J., Wang, W., Xu, Y., Wang, Y., 2018. Reconstructing South China in Phanerozoic and Precambrian. Earth-Sci. Rev. 186, 173–194.
Chaudhuri, A., Das, K., Banerjee, S., Fitzsimons, I.C.W., 2020. Detrital zircon and monazite track the source of Mesozoic sediments in Kutch to rocks of Late Neoproterozoic and Early Palaeozoic orogenies in northern India. Gondwana Res. 80, 188–201.
Chiu, H.-Y., Chung, S.-L., Wu, F.-Y., Liu, D., Liang, Y.-H., Lin, I.-J., Iizuka, Y., Xie, L.-W., Wang, Y., Chu, M.-F., 2009. Zircon U-Pb and Hf isotopic constraints from eastern Transhimalayan batholiths on the precollisional magmatic and tectonic evolution in southern Tibet. Tectonophysics 477 (1-2), 3–19.
Corfu, F., Hanchar, J.M., Hoskin, P.W.O., Kinny, P., 2003. Atlas of zircon textures. In: Zircon, Hanchar, J.M., Hoskin, P.W.O. (Eds.), Reviews in Mineralogy and Geochemistry, pp. 468–500.
Crawford, A.R., Compston, W., 1969. The age of the Vindhyan system of peninsular India. Q. J. Geol. Soc. London 125 (1-4), 351–371.
Dhar, S., Frei, R., Kramers, J.D., Nagler, T.F., Kochhar, N., 1996. Sr, Pb and Nd isotope studies and their bearing on the petrogenesis of the Jalore and Siwana complexes, Rajasthan, India. J. Geol. Soc. India 48, 151–160.
Dharma, R.C.V., Santosh, M., Kim, S.W., 2012. Cryogenian volcanic arc in the NW Indian Shield: Zircon SHRIMP U-Pb geochronology of felsic tuffs and implications for Gondwana assembly. Gondwana Res. 22, 36–53.
Eby, G.N., 1990. The A-type granitoids: a review of their occurrence and chemical characteristics and speculations on their petrogenesis. Lithos 26, 115–134.
Eby, G.N., 1992. Chemical subdivision of the A-type granitoids: petrogenetic and tectonic implications. Geology 20, 641–644.
Eby, G.N., Kochhar, N., 1990. Geochemistry and Petrogenesis of the Malani Igneous Suite, North Peninsular India. Geol. Soc. India 36, 109–130.
Frost, B.R., Barnes, C.G., Collins, W.J., Arculus, R.J., Ellis, D.J., Frost, C.D., 2001. A geochemical classification for granitic rocks. J. Petrol. 42, 2033–2048.
Fu, B., Mernagh, T.P., Kita, N.T., Kemp, A.I.S., Valley, J.W., 2008. Distinguishing magmatic zircon from hydrothermal zircon: a case study from the Gidginbung high-sulphidation Au-Ag-(Cu) deposit, SE Australia. Chem. Geol. 259, 131–142.
Griffin, W.L., Pearson, N.J., Belousova, E.A., Jackson, S.E., Achterbergh, E., Suzanne, Y. O., Shee, S.R., 2000. The Hf isotope composition of cratonic mantle: LAM-MC-ICPMS analysis of zircon megacrysts in kimberlites. Geochim. Cosmochim. Acta 64, 133–147.
Grimes, C.B., John, B.E., Kelemen, P.B., Mazdab, F.K., Wooden, J.L., Cheadle, M.J., Hanghoj, K., Schwartz, J.J., 2007. Trace element chemistry of zircons from oceanic crust: a method for distinguishing detrital zircon provenance. Geology 35, 643–646.
Grimes, C.B., Wooden, J.L., Cheadle, M.J., John, B.E., 2015. "Fingerprinting" tectono-magmatic provenance using trace elements in igneous zircon. Contrib. Miner. Petrol. 170, 46.
Hanchar, J.M., Watson, E.B., 2003. Zircon saturation thermometry. Rev. Mineral. Geochem. 53, 89–112.
Hoskin, P.W.O., Ireland, T.R., 2000. Rare earth element chemistry of zircon and its use as a provenance indicator. Geology 28, 627–630.
Hoskin, P.W.O., 2005. Trace element composition of hydrothermal zircon and the alteration of Hadean zircon from the Jack Hills, Australia. Geochim. Cosmochim. Acta 69, 637–648.
Jan, M.Q., Laghari, A., Khan, M.A., 1997. Petrography of Nagar Parkar igneous complex, Tharparkar, southeast Sindh. Geol. Bull. Univ. Peshawar 30, 227–249.
Jan, M.Q., Laghari, A., Agheem, M.H., Anjum, S., 2014. Geology and petrography of the Nagar Parkar igneous complex, southeastern Sindh, the Dinsi body. J. Himalayan Earth Sci. 47, 1–14.
Jan, M.Q., Laghari, M., Khan, M.A., Agheem, M.S., Khan, T., 2018. Petrology of calc-alkaline/adakite basement hosting A-type Neoproterozoic granites of the Malani igneous suite in Nagar Parkar, SE Sindh, Pakistan. Arab. J. Geosci. 11, 25. https://doi.org/10.1007/s12517-017-3378-1.
Khan, T., Murata, M., Rehman, H.U., Zafar, M., Ozawa, H., 2012. NagarParkar granites showing Rodinia remnants in the southeastern part of Pakistan. J. Asian Earth Sci. 59, 39–51.
Khan, T., Murata, M., Jan, M.Q., Rehman, H.U., Zafar, M., Ozawa, H., Qadir, A., Mehmood, S., 2017. Felsic dykes in the Neoproterozoic Nagar Parkar Igneous Complex, SE Sindh, Pakistan: geochemistry and tectonic setting. Arabian J. Geosci. 10, 308. https://doi.org/10.1007/s12517-017-3077-y.
Kochhar, N., 2004. Geological evolution of the Trans-Aravalli block (TAB) of the NW Indian Shield and Seychelles connection in the Late Proterozoic: evidence from plume related A-type Malani Magmatism. Geol. Survey India Spec. Publ. 84, 247–264.
Kumar, N., Kumar, N., Sharma, R., Singh, A.K., 2020. Petrogenesis and tectonic significance of the Neoproterozoic magmatism of the Tusham Ring Complex (NW Indian Shield): Insight into tectonic evolution of the Malani Igneous Suite and Rodinia Supercontinent. Geotectonics 54, 428–453.
Li, X.I., Bogdanova, S.V., Collins, A.S., Davidson, A., De Waele, B., Ernst, R.E., Fitzsimons, I.C.W., Fuck, R.A., Gladkochub, D.P., Jacobs, J., Karlstrom, K.E., Lu, S., Natapov, L.M., Pease, V., Pisarevsky, S.A., Thrane, K., Vernikovsky, V., 2008. Assembly, configuration, and break-up history of Rodinia: a synthesis. Precambr. Res. 160, 179–210.
Maas, R., Kinny, P.D., Williams, I.S., Froude, D.O., Compston, W., 1992. The Earth's oldest known crust: a geochronological and geochemical study of 3900–4200 Ma old detrital zircons from Mt. Narryer and Jack Hills, Western Australia. Geochim. Cosmochim. Acta 56, 1281–1300.
Markhand, A.H., Xia, Q., Agheem, M.H., Jia, L., 2017. U-Pb zircon dating and geochemistry of the rocks at Wadhrai body, Nagar Parkar Igneous Complex, Sindh, Pakistan. Sindh Univ. Res. J. (Sci. Ser.) 49, 1–06.
Mastoi, A.S., Yang, X., Deng, J., Hakro, A.A.A.D., 2019. Early Neoproterozoic evolution of Southeast Pakistan: evidence from geochemistry, geochronology, and isotopic composition of the Nagarparkar Igneous Complex. Int. Geol. Rev. 61, 1391–1408.
McDonough, W.F., Sun, S.S., 1995. The composition of the Earth. Chem. Geol. 120, 223–253.
Meert, J.G., Pandit, M.K., Kamenov, G.D., 2013. Further geochronological and paleomagnetic constraints on Malani (and pre-Malani) magmatism in NW India. Tectonophysics 608, 1254–1267.
Miller, C.F., McDowell, S.M., Mapes, R.W., 2003. Hot and Cold granites? Implications of zircon saturation temperatures and preservation of inheritance. Geology 31, 529–532.
Pearce, J.A., Harris, N.B., Tindle, A.G., 1984. Trace element discrimination diagrams for the tectonic interpretation of granitic rocks. J. Petrol. 25, 956–983.
Peccerillo, A., Taylor, S.R., 1976. Geochemistry of eocene calc-alkaline volcanic rocks from the Kastamonu area, Northern Turkey. Contrib. Miner. Petrol. 58, 63–81.
Pupin, J.P., 1980. Zircon and granite petrology. Contrib. Miner. Petrol. 73, 207–220.
Rehman, H.U., Lee, H.-Y., Chung, S.-L., Khan, T., O'Brien, P.J., Yamamoto, H., 2016. Source and mode of the Permian Panjal Trap magmatism: Evidence from zircon U-Pb and Hf isotopes and trace element data from the Himalayan ultrahigh-pressure rocks. Lithos 260, 286–299.
Rehman, H.U., Khan, T., Jan, M.Q., Lee, H.-Y., Chung, S.-L., Murata, M., 2018. Timing and span of the continental crustal growth in SE Pakistan: evidence from LA-ICP-MS U-Pb zircon ages from granites of the Nagar Parkar Igneous Complex. Gondwana Res. 61, 172–186.
Scherer, E.E., Whitehouse, M.J., Münker, C., 2007. Zircon as a monitor of crustal growth. Elements 3, 19–24.
Schiller, D., Finger, F., 2019. Application of Ti-in-zircon thermometry to granite studies: problems and possible solutions. Contrib. Miner. Petrol. 174, 51. https://doi.org/10.1007/s00410-019-1585-3.
Shand, S.J., 1943. In: Eruptive ROCKS. D. Van Nostrand Company, New York, p. 360.
Sharma, K.K., 2005. Malani magmatism, an extensional lithospheric tectonic origin. Geol. Soc. Am. Spec. Pap. 388, 463–476.
Shellnutt, J.G., Nguyen, D.T., Lee, H.-Y., 2020. Resolving the origin of the Seychelles microcontinent: Insight from zircon geochronology and Hf isotopes. Precambr. Res. 343, 105725.
Söderlund, U., Patchett, P.J., Vervoort, J.D., Isachsen, C.E., 2004. The ^{176}Lu decay constant determined by Lu–Hf and U-Pb isotope systematics of Precambrian mafic intrusions. Earth Planet. Sci. Lett. 219, 311–324.
Thomas, R.J., Waele, B.D., Schofield, D.I., Goodenough, K.M., Horstwood, M., Tucker, R., Bauer, W., Annells, R., Howard, K., Walsh, G., Rabarimanana, M., Rafahatelo, J.M., Ralison, A.V., Randriamananjara, T., 2009. Geological evolution of the Neoprotrerozoic Bemarivo Belt, northern Madagascar. Precambr. Res. 172, 279–300.
Torsvik, T.H., Ashwal, L.D., Tucker, R.D., Eide, E.A., 2001a. Neoproterozoic geochronology and paleogeography of the Seychelles microcontinent: the India link. Precambr. Res. 110, 47–59.
Torsvik, T.H., Carter, L.M., Ashwal, L.D., Bhushan, S.K., Pandit, M.K., Jamtveit, B., 2001b. Rodinia refined or obscured: palaeomagnetism of the Malani Igneous Suite (NW India). Precambr. Res. 65, 319–339.
de Wall, H., Pandit, M.K., Dotzler, R., Just, J., 2012. Cryogenian transpression and granite intrusion along the western margin of Rodinia (Mt. Abu region): Magnetic fabric and geochemical inferences on Neoproterozoic geodynamics of the NW Indian block. Tectonophysics 554–557, 143–158.

de Wall, H., Pandit, M.K., Sharma, K.S., Schöbel, S., Just, J., 2014. Deformation and granite intrusion in the Sirohi area, SW Rajasthan-Constraints on Cryogenian to Pan-African crustal dynamics of NW India. Precambr. Res. 254, 1–18.

de Wall, H., Pandit, M.K., Donhauser, I., Schöbel, S., Wang, W., 2018. Evolution and tectonic setting of the Malani - Nagaraparkar Igneous Suite: a Neoproterozoic Silicic-dominated Large Igneous Province i9n NW India-SE Pakistan. J. Asian Earth Sci. 160, 136–158.

Wang, W., Cawood, P.A., Zhou, M.F., Pandit, M.K., Xia, X.P., Zhao, J.H., 2017. Low-delta18O Rhyolites from the Malani Igneous Suite: A positive test for South China and NW India linkage in Rodinia. Geophys. Res. Lett. 44, 10298–10305.

Watson, E.B., Harrison, T.M., 1983. Zircon saturation revisited: temperature and composition effects in a variety of crustal magma types. Earth Planet. Sci. Lett. 64, 295–304.

Watson, E.B., Wark, D.A., Thomas, J.B., 2006. Crystallization thermometers for zircon and rutile. Contrib. Miner. Petrol. 151, 413–433.

Whalen, J.B., Curry, K.L., Chappell, B.W., 1987. A-type granites: geochemical characteristics, discrimination and petrogenesis. Contrib. Miner. Petrol. 95, 407–419.